Effects of variation in background mixing ratios of N_2, O_2, and Ar on the measurement of $\delta^{18}O$-H_2O and δ^2H-H_2O values by cavity ring-down spectroscopy

J. E. Johnson[1, 2] and C. W. Rella[3]

[1] Department of Ecology and Evolutionary Biology, University of Arizona, Tucson, AZ, USA

[2] Current address: Department of Global Ecology, Carnegie Institution, Stanford, CA, USA

[3] Picarro, Inc., Santa Clara, CA, USA

Correspondence to: J. E. Johnson (jjohnson@carnegiescience.edu)

Abstract. Cavity ring-down spectrometers have generally been designed to operate under conditions in which the background gas has a constant composition. However, there are a number of observational and experimental situations of interest in which the background gas has a variable composition. In this study, we examine the effect of background gas composition on a cavity ring-down spectrometer that measures $\delta^{18}O$-H_2O and δ^2H-H_2O values based on the amplitude of water isotopologue absorption features around 7184 cm^{-1} (L2120-*i*, Picarro, Inc.). For background mixtures balanced with N_2, the apparent $\delta^{18}O$ values deviate from true values by -0.50 ± 0.001 ‰ O_2 $\%^{-1}$ and -0.57 ± 0.001 ‰ Ar $\%^{-1}$, and apparent δ^2H values deviate from true values by 0.26 ± 0.004 ‰ O_2 $\%^{-1}$ and 0.42 ± 0.004 ‰ Ar $\%^{-1}$. The artifacts are the result of broadening, narrowing, and shifting of both the target absorption lines and strong neighboring lines. While the background-induced isotopic artifacts can largely be corrected with simple empirical or semi-mechanistic models, neither type of model is capable of completely correcting the isotopic artifacts to within the inherent instrument precision. The development of strategies for dynamically detecting and accomodating background variation in N_2, O_2, and/or Ar would facilitate the application of cavity ring-down spectrometers to a new class of observations and experiments.

1 Introduction

In most commercially available laser absorption spectrometers, the accuracy and precision of trace gas measurements are sensitive to the composition of the background gas. In this paper, we explore this issue in the context of a class of laser absorption spectrometers that is of increasing importance for environmental research, the cavity ring-down spectroscopy (CRDS) analyzers. While the CRDS analyzers can accurately and precisely measure the concentration and isotopic composition of trace gases in situations where the background gas has a constant composition, they make substantial measurement errors in situations where the background gas has a variable composition (Chen et al. 2010; Friedrichs et al. 2010; Aemisegger et al. 2012; Becker et al. 2012; Nara et al. 2012; Long et al. 2013; Volkmann and Weiler 2014). In variable backgrounds, measurement errors emerge from the interaction between two factors: first, collisional shifting and broadening of the trace gas absorption transitions; and second, the spectral acquisition and analysis strategies employed by the CRDS analyzers (Hendry et al. 2011; Gralher et al. 2016; Sprenger et al. 2017). While the fundamental collisional effects are qualitatively well-understood, their quantitative impacts on analyzer performance and the strategies needed to overcome those impacts are both incompletely understood.

To date, background effects on CRDS measurements have been reported in three different types of situations. First, calibrations for observations of the unconfined atmosphere: even though the natural levels of variability in atmospheric N_2, O_2, and Ar mixing ratios are small (i.e., ~100 ppmv), large contrasts can occur between the average composition of the atmosphere and the composition of the mixtures used for calibration (i.e., ~10,000 ppmv; Chen et al. 2010; Aemisegger et al. 2012; Nara et al. 2012; Long et al. 2013). Second, observations of confined atmospheres: for trace gas measurements in lakes, streams, oceans, and soils, the background concentrations of O_2 can vary naturally over a wide range because the rates of biological processes that produce and consume this gas can proceed more rapidly than the physical processes that control mixing with the unconfined atmosphere (i.e., ~150,000 ppmv; Friedrichs et al. 2010; Becker et al. 2012). Third, experiments with active control of background composition: some measurement techniques utilize N_2 dilution to modulate the concentrations of target trace gases in both confined and unconfined atmospheric backgrounds (Volkmann and Weiler 2014; Gralher et al. 2016).

The fundamental physical mechanisms that give rise to background gas effects on CRDS measurements are well-understood. The CRDS analyzers use high-finesse optical cavities to make ultra-sensitive quantitative absorption measurements based on infrared absorption transitions of various trace gases (O'Keefe and Deacon 1988). Two features of the absorption transitions of the trace gases are affected by collisions with the background gas: (i) the frequencies of maximum absorption intensity (i.e., denoted ν_0), and (ii) the shapes of the absorption line profiles around those central frequencies (i.e., described by $I(\nu_0)$, the maximum amplitude at ν_0, and $I(\nu_0)/2$, the full-width at half-maximum) (Demtröder 2014; Hanson et al. 2015). The former effect is termed 'shifting'; the latter effect is termed 'broadening' and/or 'narrowing.' Due to these effects, any contrast between the backgrounds used for calibrations versus observations changes the geometry of the target absorption spectrum and has the potential to introduce errors into the resulting measurements of trace gas concentrations and isotope ratios. However, whether or

not errors actually occur in any given CRDS analyzer is a function of which specific absorption spectra are targeted, and how those spectra are acquired and interpreted.

In principle, it should be possible to make CRDS measurements that are completely insensitive to background gas composition by measuring the integrated absorbance (i.e., the absorption peak area) of any isolated absorption feature in a given spectrum (Zalicki and Zare 1995). In practice, however, most current-generation CRDS analyzers are expected to exhibit some degree of sensitivity to background gas composition because they: (i) target absorption features that are not completely isolated from neighboring absorption features; (ii) measure the amplitude, rather than the area, of the target absorption features; and/or (iii) attempt to optimize measurement precision by treating lineshape parameters as fixed rather than free variables (Hodges and Lisak 2006; Hendry et al. 2011; Steig et al. 2014). On account of these design constraints, the susceptibility of different CRDS analyzers to background gas effects is a function of the identity of the specific absorption features that are targeted, the spectral acquisition approach that is used to measure those features, and the spectral analysis techniques that are used to interpret the measurements. The interactions between these factors make it difficult to predict how any particular analyzer will respond to background gas variation. As a result, experimental measurements are necessary to determine both the quantitative impacts of background gas variation on analyzer performance and the strategies needed to overcome those impacts.

The overall objective of this study is to characterize how background gas composition affects measurements of water isotopologues in one commercially-available CRDS analyzer, the L2120-*i* manufactured by Picarro, Inc. Three factors make the L2120-*i* an attractive test bed for studying background gas effects. First, a number of other types of interference have been studied in the L2120-*i*. Previous work has characterized interference from self-broadening (Schmidt et al. 2010) and from organic contaminants (Brand et al. 2009; West et al. 2010), tested algorithms for correcting for organic interference during or after analysis (Hendry et al. 2011; Schultz et al. 2011; West et al. 2011; Schmidt et al. 2012; Martín-Gómez et al. 2015; Johnson et al. 2017), and tested peripherals for pyrolizing or oxidizing organic contaminants prior to analysis (Berkelhammer et al. 2013; Martín-Gómez et al. 2015; Lazarus et al. 2016). Second, the L2120-*i* has been widely used to measure $\delta^{18}O\text{-}H_2O$ and $\delta^{2}H\text{-}H_2O$ values in situations where background variation could be relevant to the calibration procedures and/or the fundamental measurements. Examples include applications to measurements of liquid water in precipitation (Munksgaard et al. 2011), plant water (West et al. 2011), soil water (Herbstritt et al. 2012), and seawater (Munksgaard et al. 2012), as well as water vapor in the terrestrial boundary layer (Berkelhammer et al. 2013) and marine boundary layer (Steen-Larsen et al. 2014). Third, it has recently been shown that the L2120-*i* measurements are highly sensitive to the N_2/O_2, N_2/CO_2, and CO_2/O_2 composition of the background gas, and that the magnitude of the sensitivity is relevant to many observational and experimental situations (Gralher et al. 2016).

To evaluate how background gas composition impacts L2120-*i* measurements and the strategies needed to correct for those impacts, we carried out a series of experiments addressing the following questions:

(i) What are the magnitudes of the effects of variation in the mixing ratio of N_2/O_2, N_2/Ar, and O_2/Ar on the apparent $\delta^{18}O\text{-}H_2O$ and $\delta^{2}H\text{-}H_2O$ values measured by the L2120-*i* CRDS analyzer?

(ii) How are the background effects on apparent $\delta^{18}O$-H_2O and $\delta^{2}H$-H_2O values derived from the interaction between the target spectra and the spectral acquisition and analysis strategies in this instrument?

(iii) Is it practicable to develop *post hoc* calibrations for this instrument that accurately account for the effects of background variation in N_2, O_2, and/or Ar on the apparent $\delta^{18}O$-H_2O and $\delta^{2}H$-H_2O values?

2 Methods

2.1 Background gas mixtures

Background gas streams with various compositions of N_2, O_2, and Ar were generated with a mixing system (Figure 1). The mixing system consisted of four cylinders of compressed gas, thermal mass flow controllers, and a backpressure regulator upstream of the CRDS instrument inlet. Three of the cylinders contained ultra high-purity N_2, O_2, and Ar (99.999 % purity, <3 ppm H_2O, and <0.5 ppm total hydrocarbon content (THC); ALPHAGAZ 1, Air Liquide America Specialty Gases LLC, Houston, TX, USA). The fourth cylinder contained ultra high-purity air (<1 ppm H_2O, <0.01 ppm THC, <0.01 ppm CO, <0.001 ppm NO_x, <0.001 ppm SO_2; Ultrapure Air, Scott-Marrin, Inc., Riverside, CA, USA) with the N_2, O_2, and Ar composition of the natural atmosphere (i.e., 78.1 % N_2, 20.9 % O_2, 0.9 % Ar; Brewer et al. 2014; Flores et al. 2015). In the experiments, background gas mixtures were dynamically mixed from these cylinders with the mass flow controllers (FC-260 with RO-28, Tylan-Mykrolis, Allen, TX, USA). The mass flow controllers were calibrated with a bubble flow meter (25 mL Kimax bubble flow tube, Kimble-Chase, Vineland, NJ, USA) and mixing accuracy was tested for N_2/O_2 and Ar/O_2 mixtures with a galvanic oxygen sensor (MO-200, Apogee Instruments, Logan, UT, USA). With this system, the composition of each mixture could be controlled to an accuracy of ± 0.1 % of each constituent. The back-pressure regulator was used to ensure that the mixtures were supplied to the CRDS analyzer inlet at 2.5 psi above atmospheric pressure.

2.2 Liquid water standards

All of the measurements in this study were based on four vaporized liquid standards. The isotopic composition of the standards was initially established by measurement with a Finnigan Delta S Isotope Ratio Mass Spectrometer (Thermo Fisher Scientific, West Palm Beach, FL, USA) in the Environmental Isotope Laboratory, Department of Geosciences, University of Arizona (Tucson, AZ, USA). For oxygen, samples were equilibrated with CO_2 gas at approximately 15° C in an automated equilibration device coupled to the mass spectrometer. For hydrogen, samples were reacted at 750° C with Cr metal using a Finnigan H/Device coupled to the mass spectrometer. Standardization was based on distilled water standards referenced to VSMOW2 and SLAP2.

The resulting standards had the following isotopic compositions: (1) $\delta^{18}O$ = -3.74 ‰, $\delta^{2}H$ = -15.3 ‰; (2) $\delta^{18}O$ = -9.52 ‰, $\delta^{2}H$ = -62.2 ‰, (3) $\delta^{18}O$ = -14.18 ‰, $\delta^{2}H$ = -102.7 ‰, (4) $\delta^{18}O$ = -30.32 ‰, $\delta^{2}H$ = -246.7 ‰. These values were determined with analytical precision of ± 0.08 ‰ for $\delta^{18}O$ and ± 0.9 ‰ for $\delta^{2}H$. To ensure that the isotopic composition of the standards remained stable over time, they were stored in 1L amber glass bottles, with

Polyseal cone-lined screw caps, sealed with Parafilm. For CRDS measurements, 1.5 mL aliquots of each standard were pipetted into 1.8 mL glass vials with polypropylene screw caps and bonded PTFE-silicone septa (66020-950 and 46610-700, VWR, Radnor, PA, USA). To eliminate any effects from diffusive losses through the septa, each vial was measured within 24 hours of being filled and was sampled for a maximum of n = 10 successive injections.

2.3 Spectral acquisition

The CRDS analyzer used in these experiments was an L2120-*i* (Picarro, Inc., Santa Clara, CA, USA). The key components of this analyzer are a laser, a wavelength monitor, an optical cavity, and a photodetector. The laser targets H_2O absorption lines close to 7184 cm^{-1} (1392 nm). The specific lines that are utilized are 7183.685 cm^{-1} (1392.043 nm) for $^{1}H^{1}H^{16}O$, 7183.585 cm^{-1} (1392.063 nm) for $^{1}H^{1}H^{18}O$, and 7183.972 cm^{-1} (1391.988 nm) for $^{1}H^{2}H^{16}O$ (Tennyson et al. 2009; Tennyson et al. 2010; Tennyson et al. 2013). Operationally, the analyzer scans the laser across these features, recording absorption loss as a function of optical frequency (spectrograms). To generate each frequency and absorption pair, light from the laser is directed into the optical cavity, the frequency is determined by the wavelength monitor, and the power in the cavity is monitored with a photodetector detecting light leaking through one of the mirrors. The absorption is quantified based on the rate at which the light intensity decays (i.e., 'rings down') when the laser is turned off (Crosson 2008).

Since the absorbance measurements are of gas-phase H_2O, a front-end peripheral must be used to convert liquid-phase standards into the gas-phase (Gupta et al. 2009). For this study, the L2120-*i* analyzer was equipped with a V1102-i high-precision vaporizer (Picarro, Inc., Santa Clara, CA, USA) and autosampler (HTC PAL, Leap Technologies, Carrboro, NC, USA). To ensure stable performance, the analyzer, vaporizer, and autosampler were installed in an air-conditioned laboratory where the air temperature was maintained at 20.0 ± 1.7° C. All of the measurements were performed in the air carrier mode, and with the vaporizer running at 110°C. Injections were made on a 9 minute cycle, using a 10 uL syringe (SGE 10R-C/T-5/0.47C, Trajan Scientific Americas, Inc., Austin, TX, USA) which was rinsed twice in N-methyl-2-pyrrolidone (99.5 %, Acros Organics, Fisher Scientific, Pittsburgh, PA, USA) before each injection.

2.4 Spectral analysis

In the L2120-*i*, the spectrograms are interpreted with a non-linear curve fitting routine based on the Levenberg-Marquardt algorithm. The analysis is conceptually similar to that utilized in the earlier generation L1102-*i* analyzers (Hendry et al. 2011), but some details differ. Briefly, the fitting routine compares each measured spectrogram to a modeled spectrogram and adjusts the model parameters in order to minimize the residual error. The modeled spectrogram represents a mixture of $^{1}H^{1}H^{16}O$, $^{1}H^{1}H^{18}O$, and $^{1}H^{2}H^{16}O$ in a pure water standard (i.e., one that was evaluated in a zero air background and had an isotopic composition near $\delta^{18}O$ = 0 ‰ and $\delta^{2}H$ = 0 ‰). The fitting routine compares this modeled spectrogram to the measured spectrogram in three stages.

In the first stage, the fitting routine varies the amounts of $^{1}H^{1}H^{16}O$, $^{1}H^{1}H^{18}O$, and $^{1}H^{2}H^{16}O$, the centration and scale of the frequency axis, the absolute value and slope of the baseline, the linewidth, and the amounts of several potential organic contaminants (CH_4, C_2H_6, and MeOH). This fit determines the observed centration and

scale of the frequency axis ('h2o_shift' and 'h2o_squish_a'), the observed linewidth ('h2o_y_eff_a'), and the linewidth expected for the observed amount of $^1H^1H^{16}O$ in an air background ('h2o_y_eff'). The second and third stages of fitting then make different assumptions about the presence of organic contaminants.

In the second stage, the fitting routine assumes that there is no organic contamination. The centration and scale of the frequency axis are fixed based on the results of the first stage ('h2o_shift' and 'h2o_squish_a') and the effective linewidth is fixed based on the amount of $^1H^1H^{16}O$ ('h2o_y_eff'). The free parameters are the amounts of $^1H^1H^{16}O$, $^1H^1H^{18}O$, and $^1H^2H^{16}O$, as well as the absolute value and slope of the baseline. This fit determines the reported residuals ('standard_residuals'), baseline ('standard_base'), baseline slope ('standard_slope'), H_2O mixing ratio (from the amplitude of the $^1H^1H^{16}O$ peak) and the $\delta^{18}O$ and δ^2H values (from the ratios of the amplitudes of the $^1H^1H^{16}O$, $^1H^1H^{18}O$, and $^1H^2H^{16}O$ peaks).

In the third stage, the fitting routine allows for the possibility of organic contamination. Here, the centration and scale of the frequency axis are fixed based on the results of the first stage ('h2o_shift' and 'h2o_squish_a') and the effective linewidth is fixed based on the observed linewidth ('h2o_y_eff_a'). The free parameters are the amounts of the organic contaminants, the amounts of $^1H^1H^{16}O$, $^1H^1H^{18}O$, and $^1H^2H^{16}O$, as well as the absolute value and slope of the baseline. This fit determines the reported 'organic-corrected' residuals ('organic_res'), baseline ('organic_base'), baseline slope ('organic_slope'), and $\delta^{18}O$ and δ^2H values (from the ratios of the organic-corrected amplitudes of the three peaks).

2.5 Experimental design

2.5.1 Characterizing background gas effects

We performed three experiments to characterize the effects of variation in the mixing ratios of N_2/O_2, N_2/Ar, and O_2/Ar, respectively. In each experiment, we generated five backgrounds from the two gases (i.e., 0/100, 25,75, 50/50, 75/25, and 100/0; in %). In each background, we measured the four liquid standards across a range of injection volumes (i.e., 400-2400 nL, in eleven steps of 200 nL each). For the most isotopically enriched standard, we performed three replicate injections at each injection volume; for the other three standards, we performed a single injection at each injection volume. At each transition between standards, we inserted fifteen additional injections to allow for full equilibration and eliminate any carryover effects. At each transition between backgrounds, we inserted four additional injections in UHP N_2 to check for instrumental drift. Both the transition injections and the drift check injections were analyzed solely for quality control and quality assurance purposes. For the primary analyses of N_2, O_2, and Ar effects, the remaining injections yielded a total sample size of n = 330 per experiment, and n = 990 across the three experiments.

2.5.2 Evaluating corrections for background gas effects

We performed a fourth experiment to test whether the background effects observed in the pure gases (N_2, O_2, Ar) and binary gas mixtures (N_2/O_2, N_2/Ar, and O_2/Ar) could be used to predict the effects in a ternary mixture representing natural atmospheric composition (N_2/O_2/Ar). In this experiment, we used the ultra high-purity whole air

as the background and measured the same four liquid standards across a range of injection volumes (i.e., 600, 1200, 2000, 3000 nL). For each standard, we performed three replicate injections at each injection volume. At each transition between standards, we again inserted fifteen additional injections to allow for full equilibration and eliminate any carryover effects. The transition injections were analyzed solely for quality control and quality assurance purposes, such that the remaining injections yielded a total sample size of n = 240.

2.6 Data analysis

Since the default configuration of the L2120-*i* software does not write all of the intermediate spectral parameters to the liquid injection output files, we retrieved the analyzer's complete raw data files for the duration of these experiments from the archive directory, and calculated the mean and standard deviation of each parameter over the intervals defined by the injection peak-picking algorithm. Statistical analyses were then performed using the open-source statistical software, R (R Core Team, 2016). Briefly, the data were fit to a series of multivariate linear models using the 'lm()' function from base R, and the fit was evaluated in terms of the residual standard error (RSE), adjusted R^2 and F-test P-value. More details of each analysis are provided in the following sections.

2.6.1 Notation

For all samples, the relative abundances of the heavy and light isotopologues were expressed with the dimensionless isotope ratios:

$$R_{sample} = [^1H^1H^{18}O]/[^1H^1H^{16}O], \text{ or } [^1H^2H^{16}O]/[^1H^1H^{16}O], \quad (1)$$

The isotope ratios were normalized relative to the international standard VSMOW (Vienna Standard Mean Ocean Water):

$$\delta^{18}O \text{ or } \delta^2H \text{ (‰)} = (R_{sample}/R_{VSMOW} - 1), \quad (2)$$

where R_{sample} and R_{VSMOW} represent the ratios of the abundance of the heavy and light isotopologues in the samples and international standard, respectively.

To refer to calibrated $\delta^{18}O$ and δ^2H values as determined by IRMS, we use the subscript 'true' (i.e., $\delta^{18}O_{true}$ and δ^2H_{true}). To refer to uncalibrated $\delta^{18}O$ and δ^2H values as determined by CRDS, we use the subscript 'apparent' (i.e., $\delta^{18}O_{apparent}$ and $\delta^2H_{apparent}$).

2.6.2 Magnitude of background effects

To visualize the effects of variation in the mixing ratios of N_2/O_2, N_2/Ar, and O_2/Ar on the apparent isotopic composition of H_2O, we plotted the background composition against the difference between the apparent and true isotopic composition of each sample (i.e., $\Delta\delta^{18}O = \delta^{18}O_{apparent} - \delta^{18}O_{true}$ and $\Delta\delta^2H = \delta^2H_{apparent} - \delta^2H_{true}$). To

quantify the magnitude of the effects of background variation on the apparent isotopic composition of H_2O, we then fit a series of multivariate linear models. First, we examined the measurements in the pure background gases. For each pure background, we described variation in the apparent isotopic composition of water with a multivariate linear model of the form:

$$Y = \beta_0 + X_1 \cdot \beta_1 + X_2 \cdot \beta_2 + X_3 \cdot \beta_3 + X_4 \cdot \beta_4, \quad (3)$$

where Y is the apparent isotopic composition of water ($\delta^{18}O_{apparent}$, $\delta^{2}H_{apparent}$; in units ‰), X_1 is the true isotopic composition of water ($\delta^{18}O_{true}$, $\delta^{2}H_{true}$; in units ‰), X_2 is the water mixing ratio (H_2O; in units %), X_3 is the inverse of the water mixing ratio ($1/X_2$), X_4 is the square of the water mixing ratio (X_2^2), and β_0, β_1, β_2, β_3, and β_4 are the regression coefficients. This functional form provides a good description of the sensitivity of the apparent isotopic composition of water to the water mixing ratio in the L2120-*i* and similar analyzers from the same manufacturer (Rella 2010; Rella et al. 2015). Next, we examined the measurements in the binary mixtures. For each binary mixture, we added an additional term to capture the effects of background variation:

$$Y = \beta_0 + X_1 \cdot \beta_1 + X_2 \cdot \beta_2 + X_3 \cdot \beta_3 + X_4 \cdot \beta_4 + X_5 \cdot \beta_5, \quad (4)$$

where X_5 is the mixing ratio of either O_2 or Ar (in units %) and β_5 is the corresponding regression coefficient. Finally, we combined all of the binary mixtures into a composite dataset. For this composite dataset, we added two terms to capture the effects of background variation:

$$Y = \beta_0 + X_1 \cdot \beta_1 + X_2 \cdot \beta_2 + X_3 \cdot \beta_3 + X_4 \cdot \beta_4 + X_5 \cdot \beta_5 + X_6 \cdot \beta_6, \quad (5)$$

where X_5 and X_6 are the mixing ratios of O_2 and Ar (in units %) and β_5 and β_6 are the corresponding regression coefficients.

2.6.4 Geometric basis of background effects

To visualize the geometric basis of the background effects, we plotted the $\Delta\delta^{18}O$ and $\Delta\delta^{2}H$ values against three parameters calculated during the second stage of fitting ('standard_residuals', 'standard_base', 'standard_slope'), three parameters calculated during the first stage of fitting and included as fixed values during the second stage ('h2o_shift', 'h2o_squish_a', 'h2o_y_eff'), and one parameter calculated during the first stage of fitting and omitted during the second stage ('h2o_y_eff_a'). To visualize the interactions between the background composition and the H_2O mixing ratio, we also plotted each parameter against the H_2O mixing ratio ('h2o_ppmv'). We then formulated a series of semi-mechanistic models to test which of the seven spectral parameters was the best predictor of the isotopic error terms. Each model described variation in the apparent isotopic composition of water as:

$$Y = \beta_0 + X_1 \cdot \beta_1 + X_2 \cdot \beta_2 + X_3 \cdot \beta_3 + X_4 \cdot \beta_4 + X_7 \cdot \beta_7, \quad (6)$$

where X_7 is one of the seven spectral parameters and β_7 is the corresponding regression coefficient. N.B., this expression is analogous to Eq. 5 with the exception that one of the spectral parameters (X_7) has been substituted for the mixing ratios of O_2 and Ar (X_5 and X_6).

2.6.5 Prediction of background effects in a ternary mixture

We used the empirical model described by Eq. (5) and the semi-mechanistic model described by Eq. (6) derived from the measurements of the standards in binary mixtures to predict the apparent isotopic composition of the standards within the ternary gas mixture. To evaluate how water vapor self-broadening vs. background-broadening affected model performance, we assessed model skill across the entire range of water vapor mixing ratios (*i.e.*, n = 240 analyses for 2,500 ppmv ≤ H_2O ≤ 35,000 ppmv), as well as within a restricted subset of intermediate-range water vapor mixing ratios (*i.e.*, n = 116 analyses for 10,000 ppmv ≤ H_2O ≤ 25,000 ppmv). To provide a benchmark for evaluating the 1σ precision of each empirical and semi-mechanistic model, we calculated the long-term 1σ precision of the L2120-*i* analyzer using an independent dataset comprised of previous measurements of the same set of standards, across the same range of water mixing ratios, and in the same type of ultra-high purity air that was used to test the two models.

3 Results

3.1 Magnitude of background effects

Across the N_2/O_2, N_2/Ar, and O_2/Ar mixing experiments, the average differences between the apparent and true isotopic composition of the standards are -18.45 ± 20.02 ‰ for $\Delta\delta^{18}O$ values and 24.5 ± 17.1 for $\Delta\delta^{2}H$ values (i.e., for n = 990; Figure 2). The variation in $\Delta\delta^{18}O$ and $\Delta\delta^{2}H$ values is partially due to the variation in the mixing ratio of H_2O, and partially due to the variation in the mixing ratios of N_2/O_2, N_2/Ar, and O_2/Ar. For $\delta^{18}O$ values, the range of H_2O mixing ratios that was evaluated has effects of smaller magnitude than the ranges of N_2/O_2, N_2/Ar, and O_2/Ar mixing ratios that were evaluated (Figure 2, a-c). For $\delta^{2}H$ values, both factors have effects of similar magnitude (Figure 2, d-f).

Within the subsets of measurements made in pure N_2, O_2, and Ar, Eq. (3) accounts for the effects of the H_2O mixing ratio with overall precision ranging between 0.37-1.16 ‰ for $\delta^{18}O$ values and 2.3-3.7 for $\delta^{2}H$ values (Table 1). The structure of the best-fit models varies between isotopologues and between backgrounds, with all three of the H_2O mixing ratio-dependent parameters significant in some cases and none significant in others (Table 1). Within the models where the coefficient describing the first-order response to the H_2O mixing ratio, β_2, has significant explanatory power, it tends to have a negative sign for $\delta^{18}O$ values (Table 1; Models 1, 3) and a positive sign for $\delta^{2}H$ values (Table 1; Model 4).

Within each of the binary mixtures, Eq. (4) accounts for the combined effects of the H_2O mixing ratio and the N_2/O_2, N_2/Ar, and O_2/Ar mixing ratios with overall precision ranging between 0.33-0.62 ‰ for $\delta^{18}O$ values and

3.2-5.2 for δ^2H values (Table 2). Within these models, the coefficient describing the first-order response to the O_2 or Ar mixing ratio, β_5, also tends to have a negative sign for $\delta^{18}O$ values (Table 2; Models 1, 3, 5) and a positive sign for δ^2H values (Table 2; Models 2, 4, 6). For both $\delta^{18}O$ and δ^2H values, the magnitude of β_5 in the O_2/Ar experiment is equivalent to the difference in the magnitude of β_5 in the N_2/O_2 experiment versus in the N_2/Ar experiment (Table 2).

When all three experiments are combined into a single dataset, Eq. (5) accounts for the combined effects of the H_2O mixing ratio and the N_2/O_2, N_2/Ar, and O_2/Ar mixing ratios with overall precision of 0.62 ‰ for $\delta^{18}O$ values and 3.6 ‰ for δ^2H values (Table 3). Within these models, the coefficients describing the first-order response to the O_2 and Ar mixing ratios, β_5 and β_6, have negative signs for $\delta^{18}O$ values (Table 3; Model 1) and positive signs for δ^2H values (Table 3; Model 2). For both $\delta^{18}O$ and δ^2H values, the sensitivity to Ar is relatively higher than the sensitivity to O_2 (Table 3; Models 1, 2). In absolute terms, the apparent $\delta^{18}O$ values deviate from true values by -0.50 ± 0.001 ‰ O_2 $\%^{-1}$ and -0.57 ± 0.001 ‰ Ar $\%^{-1}$, respectively (Table 3; Model 1). The apparent δ^2H values deviate from true values by 0.26 ± 0.004 ‰ O_2 $\%^{-1}$ and 0.42 ± 0.004 ‰ Ar $\%^{-1}$, respectively (Table 3; Model 2).

3.2 Geometric basis of background effects

Overall, the relationships between the isotopic error terms and the spectral parameters have two shared features. First, the background composition has consistent effects across the three experiments. For each spectral fitting parameter, the patterns observed in the O_2/Ar experiment are equivalent to the difference in the patterns observed in the N_2/O_2 experiment versus in the N_2/Ar experiment (i.e., for $\delta^{18}O$ values, compare differences between panels (a) and (b) to (c) in Figures 3-9; for δ^2H values, compare differences between panels (d) and (e) to (f) in Figures 3-9). Second, for those spectral parameters that have significant linear relationships with the isotopic error terms, the relative sensitivities of the two isotopologues to any given spectral parameter always have opposing signs. The apparent $\delta^{18}O$ values become more depleted with decreases in the absolute value of the baseline (Figure 4, a-c), increases in the slope of the baseline (Figure 5, a-c), increases in the frequency scale correction parameter (Figure 7, a-c), and decreases in the free linewidth parameter (Figure 9, a-c). In contrast, the apparent δ^2H values become more enriched with the analogous changes in those parameters (Figures 3-9, d-f).

Beyond these shared features, there is substantial variation between the spectral parameters in terms of the complexity of their relationships to the isotopic error terms. The spectral residuals do not have a linear relationship with the isotopic error terms: although maximum values of the residuals are usually associated with maximum values of the isotopic error terms, minimum values of the residuals are associated with the full range of values of the isotopic error terms (Figure 3, a-f). The absolute value of the baseline and the baseline slope each have significant linear relationships with the isotopic error terms, but also have large amounts of variation that are not directly related to the isotopic error terms (Figures 4-5, a-f). The frequency shift parameter does not have significant relationships with the isotopic error terms (Figure 6, a-f), but the frequency scale correction parameter does have significant linear relationships with the isotopic error terms (Figure 7, a-f). Analogously, the fixed linewidth parameter does not have significant relationships with the isotopic error terms (Figure 8, a-f), but the free linewidth parameter does have significant relationships with the isotopic error terms (Figure 9, a-f).

The complexity of the relationships between the spectral parameters and isotopic error terms is driven by interactions between the background composition and the H_2O mixing ratios (Figures 10-11). For the spectral residuals, baseline, and baseline slope, there is a multiplicative interaction between the background composition and H_2O mixing ratio: at the lowest H_2O mixing ratios, variation in background composition has the smallest effects on the spectral residuals, baseline, and baseline slope; at the highest H_2O mixing ratios, the opposite is true (Figure 10, a-c). For the frequency scale correction and free linewidth parameters, there is an additive interaction between the background composition and H_2O mixing ratio: regardless of the H_2O mixing ratio, variation in background composition has similar effects on the frequency scale correction and free linewidth parameters (Figure 11, b, d). For the frequency shift and fixed linewidth parameters, there is no interaction between the background composition and H_2O mixing ratio: both parameters vary with the H_2O mixing ratio, but those relationships are insensitive to the background composition (Figure 11, a, c).

In the semi-mechanistic models (Eq. 6), the free linewidth parameter is a better predictor than any of the other spectral parameters (Table 4). The models based on the free linewidth parameter account for the combined effects of the H_2O mixing ratio and the N_2/O_2, N_2/Ar, and O_2/Ar mixing ratios with overall precision of 2.54 ‰ for $\delta^{18}O$ values and 4.4 ‰ for δ^2H values (Table 4). In these models, the coefficient describing the first-order response to the free linewidth parameter, β_7, has a positive sign for $\delta^{18}O$ values (Table 4; Model 7) and a negative sign for δ^2H values (Table 4; Model 14). The second-best predictor is the frequency scale correction parameter (Table 4). The models based on the frequency scale correction parameter have overall precision of 6.72 ‰ for $\delta^{18}O$ values and 4.9 ‰ for δ^2H values (Table 4). For this parameter, the β_7 coefficient has a negative sign for $\delta^{18}O$ values (Table 4; Model 6) and a positive sign for δ^2H values (Table 4; Model 13).

3.3 Prediction of background effects in a ternary mixture

For $\delta^{18}O$, the empirical model predicts the apparent $\delta^{18}O$ values with a 1σ precision of ± 0.99 ‰, whereas the semi-mechanistic model predicts the apparent $\delta^{18}O$ values with a 1σ precision of ± 1.68 ‰ (n = 240; Table 5). When the test measurements in the ternary gas mixture are restricted to intermediate mixing ratios in the range of 10,000-25,000 ppmv H_2O, these values improve to ± 0.80 ‰ and ± 1.21 ‰, respectively (n = 116; Table 5). For δ^2H, the empirical model predicts the apparent δ^2H values with a 1σ precision of ± 3.1 ‰, whereas the semi-mechanistic model predicts the apparent δ^2H values with a 1σ precision of ± 3.0 ‰ (Table 5). For intermediate mixing ratios in the range of 10,000-25,000 ppmv H_2O, these values improve to ± 2.0 ‰ and ± 2.1 ‰, respectively (n = 116; Table 5). As a benchmark for comparison, the average long-term 1σ precision of this L2120-*i* analyzer is ± 0.24 ‰ for $\delta^{18}O$ values and ± 1.4 ‰ for δ^2H values across the range of mixing ratios from 2,500 - 35,000 ppmv H_2O.

4 Discussion

4.1 What are the magnitudes of the effects of variation in the mixing ratio of N_2/O_2, N_2/Ar, and O_2/Ar on the apparent $\delta^{18}O$-H_2O and δ^2H-H_2O values measured by the L2120-*i* CRDS analyzer?

Across the range of backgrounds considered in this study, variation in the N_2/O_2, N_2/Ar, and O_2/Ar ratios has substantial effects on the apparent isotopic composition of water reported by the L2120-*i* (Figure 2). For $\delta^{18}O$, combining the long-term 1σ precision of the analyzer (± 0.24 ‰) and the magnitude of the sensitivities to O_2 and Ar relative to N_2 (i.e., -0.50 ± 0.001 ‰ O_2 %$^{-1}$ and -0.57 ± 0.001 ‰ Ar %$^{-1}$; Table 3) implies that variation over the thresholds of ± 0.48 % O_2 or ± 0.42 % Ar is expected to result in detectable oxygen isotope errors. For δ^2H, combining the long-term 1σ precision of the analyzer (± 1.4 ‰) and the magnitude of the sensitivities to O_2 and Ar relative to N_2 (i.e., 0.26 ± 0.004 ‰ O_2 %$^{-1}$ and 0.42 ± 0.004 ‰ Ar %$^{-1}$; Table 3) implies that variation over the thresholds of ± 5.4 % O_2 or ± 3.3 % Ar is expected to result in detectable hydrogen isotope errors.

The only previous measurements available for direct comparison to these results are those of Gralher et al. (2016). In binary N_2/O_2 mixtures, Gralher et al. (2016) found that a different L2120-*i* analyzer exhibited a sensitivity of -0.56 ‰ O_2 %$^{-1}$ for $\delta^{18}O$ values and a sensitivity of 0.42 ‰ O_2 %$^{-1}$ for δ^2H values (i.e., see Figure 2 in that reference). Overall, the Gralher et al. (2016) values are more similar to our binary N_2/Ar sensitivities (i.e., for $\delta^{18}O$-H_2O, -0.56 ± 0.001 ‰ Ar %$^{-1}$; for δ^2H-H_2O, 0.43 ± 0.005 ‰ Ar %$^{-1}$; Table 2) than our binary N_2/O_2 sensitivities (i.e., for $\delta^{18}O$-H_2O, -0.50 ± 0.001 ‰ O_2 %$^{-1}$; for δ^2H-H_2O, 0.26 ± 0.009 ‰ O_2 %$^{-1}$; Table 2). This is unexpected, and the responsible mechanisms are not entirely clear.

Since the Gralher et al. (2016) sensitivities were derived from measurements across narrow ranges of H_2O mixing ratios (i.e., ~ 17,000 ppmv) and O_2 mixing ratios (i.e., 0-20%), one possible explanation is that the wider ranges used in our study could be responsible for the different sensitivity estimates. Subsetting our dataset to the range of H_2O mixing ratios used by Gralher et al. (2016) yields N_2/O_2 sensitivities equivalent to those reported in Table 2. However, subsetting our dataset to the range of O_2 mixing ratios used by Gralher et al. (2016) does yield N_2/O_2 sensitivities in much closer agreement with those authors' results (i.e., for $\delta^{18}O$, -0.54 ± 0.003 ‰ O_2 %$^{-1}$; for δ^2H, 0.38 ± 0.002 ‰ O_2 %$^{-1}$). This suggests that the differences in the sensitivity estimates are derived from the different ranges of N_2/O_2 mixing ratios used in the two studies.

4.2 How are the background effects on the apparent $\delta^{18}O$-H_2O and δ^2H-H_2O values derived from the interaction between the target spectra and the spectral acquisition and analysis strategies in this instrument?

Overall, the strongest direct effect of the background gas composition is on the effective linewidth of the target absorption features. In pure N_2 backgrounds, the actual value of the effective linewidth is greater than the value prescribed for air backgrounds. The spectral analysis algorithm attempts to compensate for this mis-specification of the peak shape by decreasing the frequency scale correction parameter (i.e., h2o_squish_a), but the peak shape mis-specification persists in spite of the frequency scale adjustments (i.e., h2o_y_eff_a > h2o_y_eff). As a result, the amplitudes of the absorption peaks are systematically overestimated (Figure 12, a). The degree of overestimation increases in the order $^1H^2H^{16}O$ < $^1H^1H^{16}O$ < $^1H^1H^{18}O$, with the result that the $\Delta\delta^{18}O$ values are positive and the $\Delta\delta^2H$ values are negative. In pure O_2 and Ar backgrounds, the actual value of the effective linewidth

is less than the value prescribed for air backgrounds. Here, the spectral analysis algorithm attempts to compensate by increasing the frequency scale correction parameter (i.e., h2o_squish_a), but the peak shape mis-specification again persists (i.e., h2o_y_eff_a < h2o_y_eff). In these backgrounds, the amplitudes of the absorption peaks are systematically underestimated (Figure 12, b). The degree of underestimation increases in the order $^{1}H^{2}H^{16}O$ < $^{1}H^{1}H^{16}O$ < $^{1}H^{1}H^{18}O$, such that the $\Delta\delta^{18}O$ values are negative and the $\Delta\delta^{2}H$ values are positive. On the one hand, the tendency for the absorption spectrum to be broader in N_2, intermediate in O_2, and narrower in Ar is entirely consistent with the normal behavior of isolated water vapor absorption lines (Buldyreva et al. 2011). On the other hand, it is not entirely clear why the $^{1}H^{2}H^{16}O$, $^{1}H^{1}H^{16}O$, and $^{1}H^{1}H^{18}O$ lines exhibit increasing susceptibility to peak shape mis-specification.

One possible explanation is that the differential errors are derived from indirect effects of the background gas. The three water vapor absorption lines that are targeted by the L2120-*i* are all characterized by relatively low line-strengths, but they sit on the upper 'wings' of lower-frequency water vapor absorption lines that are characterized by much higher line-stengths (i.e., at ν_0 = 7181.156, 7182.209, and 7182.950 cm^{-1}; (Lisak et al. 2009); Figure 12, c). The broadening, narrowing, and shifting of these strong off-screen lines appear to be the major control on variation in the spectral residuals, spectral baseline, and baseline slope parameters. Specifically, N_2-induced increases in the width of the offscreen lines seem to decrease the baseline slope and increase the absolute value of the baseline, whereas O_2- and Ar-induced decreases in the width of the offscreen lines seem to increase the baseline slope and decrease the absolute value of the baseline. Since the target $^{1}H^{1}H^{18}O$ line is at a lower frequency than the target $^{1}H^{1}H^{16}O$ line, and the target $^{1}H^{1}H^{16}O$ line is in turn at a lower frequency than the target $^{1}H^{2}H^{16}O$ line, the baseline perturbations from the off-screen lines increase in the same rank order as, and could be responsible for, the differential peak shape mis-specifications (i.e., $^{1}H^{2}H^{16}O$ < $^{1}H^{1}H^{16}O$ < $^{1}H^{1}H^{18}O$).

However, proximity to the off-screen features is not the only possible explanation for the differential peak shape mis-specifications. For example, the $^{1}H^{2}H^{16}O$, $^{1}H^{1}H^{16}O$, and $^{1}H^{1}H^{18}O$ lines also vary in line strength in the order $^{1}H^{2}H^{16}O$ < $^{1}H^{1}H^{16}O$ < $^{1}H^{1}H^{18}O$ (Tennyson et al. 2009; Tennyson et al. 2010; Tennyson et al. 2013). As a result, a second possible explanation is that the differential susceptibility to peak shape mis-specification is primarily a function of line strength. This interpretation is supported by the fact that the largest negative $\Delta\delta^{18}O$ errors occur in the most $\delta^{18}O$-enriched standard (i.e., where the difference in amplitude between the $^{1}H^{1}H^{16}O$ and $^{1}H^{1}H^{18}O$ lines is maximized), whereas the largest positive $\Delta\delta^{2}H$ errors occurr in the most $\delta^{2}H$-depleted standard (i.e., where the difference in amplitude between $^{1}H^{2}H^{16}O$ and $^{1}H^{1}H^{16}O$ is maximized). Nonetheless, it could also be the case that the differential susceptibility to peak shape mis-specification is a function of a combination of several of the above mechanisms, or other undefined mechanisms. To definitively distinguish among these possibilities, it would be necessary to have accurate measurements of the broadening, narrowing, and shifting coefficients for each of the individual lines in the target spectrum, rather than the 'effective' coefficients that the L2120-*i* calculates for the composite spectrum.

4.3 Is it practicable to develop *post hoc* calibrations for this instrument that accurately account for the effects of background variation in N_2, O_2, and/or Ar on the apparent $\delta^{18}O$-H_2O and δ^2H-H_2O values?

On the one hand, the majority of the background-induced isotope artifacts can be corrected with either simple empirical or semi-mechanistic models (Table 5). The success of both types of models is likely a reflection of the fact that the collisional broadening, narrowing and shifting coefficients of any given absorption line in a mixed background can all be satisfactorily described as linear combinations of the corresponding coefficients in pure backgrounds (Buldyreva et al. 2011). On the other hand, neither type of model is capable of completely correcting the isotopic artifacts to within the inherent instrument precision (Table 5). Although the loss of precision for δ^2H values is similar for the semi-mechanistic and empirical corrections, the loss of precision for $\delta^{18}O$ values is slightly greater for the semi-mechanistic corrections than for the empirical corrections. In combination, these findings indicate that there are several feasible approaches for *post hoc* calibrations of CRDS measurements that accurately account for background variation in N_2, O_2, and/or Ar, but that all currently tradeoff with measurement precision. Since the precision of the $\delta^{18}O$ and δ^2H measurements in turn controls the precision of the derived deterium excess parameter (i.e., *d*-excess = $\delta^2H - 8 \cdot \delta^{18}O$), this has important implications for the range of strategies that can be used to calibrate CRDS analyzers for $\delta^{18}O$, δ^2H, and *d*-excess measurements. Different types of strategies are likely to be required for measurements: (i) in the atmosphere, and (ii) in other settings.

For atmospheric applications, there are likely to be systematic inaccuracies in $\delta^{18}O$ and *d*-excess values if 'synthetic air' is used as a calibration background without accounting for the fact that these N_2/O_2 mixtures lack Ar and may exhibit cylinder-to-cylinder variation in N_2 versus O_2 content. For example, these effects may explain the cylinder-to-cylinder calibration shifts observed when Air Liquide's 'ALPHAGAZ 1' has been used as a calibration background for atmospheric observations (e.g., see Aemisegger et al. (2012) and Casado et al. (2016)). To address this issue, previous studies have recommended performing CRDS calibrations for atmospheric observations in natural air backgrounds (Chen et al. 2010; Aemisegger et al. 2012; Nara et al. 2012; Long et al. 2013). The results of the current study corroborate this approach, but indicate that it represents only one of two alternatives. The other approach is performing calibration measurements in a background that does not conform to atmospheric composition, and using sensitivity experiments of the sort reported here to develop transfer functions that translate between the calibration and observation backgrounds (i.e., similar to Eq. 5). Despite its relatively lower precision, this approach may nonetheless represent the preferred strategy for applications where it is difficult or impossible to obtain sufficiently purified natural air for calibration.

For marine, freshwater, and soil applications, there are likely to be systematic inaccuracies in $\delta^{18}O$, δ^2H, and *d*-excess values of liquid and vapor samples if the calibration strategy does not account for dynamic variation in the O_2 content of the measurement background. For example, marine dissolved oxygen levels range from supersaturated during high-productivity periods in upwelling zones (Schmidt and Eggert 2016), to hypoxic during harmful algal blooms in coastal zones (O'Boyle et al. 2016), to anoxic in deep water oxygen minimum zones (Larsen et al. 2016). To address this type of dynamic variation in background O_2 content, Friedrichs et al. (2010) and Becker et al. (2012) have demonstrated that linewidth information from CRDS measurements of CO_2 and $\delta^{13}C$-CO_2 can be used to both detect and correct for O_2–induced errors. The results of the current study indicate that an analogous

approach can be used with the L2120-*i* (i.e., based on Eq. 6), although doing so will further reduce the precision of the $\delta^{18}O$ values. It is likely that the spectroscopically-based corrections are less successful in the L2120-*i* because the 7183-7184 cm^{-1} region is congested, and the fitting algorithm does not perform individual fits on the target H_2O isotopologue peaks. In contrast, the EnviroSense 2050 analyzer used by Friedrichs et al. (2010) and Becker et al. (2012) targeted a relatively uncongested spectral region (6251-6252 cm^{-1}) and performed individual fits on each of the target CO_2 isotopologue peaks.

Looking forward, the most straightforward approach to overcome the tradeoff between background stability and measurement precision would be to develop new spectral acquisition and analysis strategies for CRDS measurements that can accommodate dynamic variation in the composition of the background gas. Considering that the integrated absorbance of isolated features in CRDS spectra is expected to be conserved regardless of the degree of broadening, narrowing, or shifting induced by the background gas (Zalicki and Zare 1995), the next generation of CRDS analyzers that quantify absorption based on peak areas may be less sensitive to background variation than those that quantify absorption based on peak amplitudes (Steig et al. 2014). A recent report of the insensitivity of off-axis integrated cavity output spectroscopy (OA-ICOS) to background variation from 1-5 % CO_2 is consistent with this idea (Sprenger et al. 2017). However, while measurements of integrated absorbance may be necessary for limiting sensitivity to background effects, they are unlikely to be sufficient for entirely eliminating sensitivity to background effects. To achieve this objective, it may be useful to introduce spectral fitting strategies in which all of the lineshape parameters are treated as free rather than fixed variables. Such 'calibration-free' spectral fitting strategies have been recently been developed for high-temperature and high-pressure applications in energy research, and these might serve as models for lower-temperature and lower-pressure applications in environmental research (Sun et al. 2013; Goldenstein et al. 2014; Sur et al. 2015; Goldenstein et al. 2017).

5 Conclusions

Due to the sensitivity of the L2120-*i* to background gas composition, this model CRDS analyzer is best suited for applications in which the background O_2 and Ar mixing ratios vary by no more than a maximum of 0.5 %, and ideally by less than 0.1 %. Calibration strategies should be designed to ensure that if there is any contrast between the background used for calibration and measurement, it is no greater than this threshold. For observations or experiments in which the background O_2 and Ar mixing ratios vary by more than 0.5 %, the measurements of the L2120-*i* will include systematic errors that are derived from the broadening, narrowing, and shifting of both the target absorption lines and strong neighboring lines. If the composition of the variable background is known, the errors can be accurately corrected with the empirical model described by Eq. (5). If the composition of the variable background is unknown, the errors can also be accurately corrected with the semi-mechanistic model described by Eq. (6). In either case, accuracy and precision will be maximized by calculating the coefficients for Eq. (5) or (6) from a calibration dataset that encompasses the full range of variation in N_2, O_2, and/or Ar mixing ratios, H_2O mixing ratios, and $\delta^{18}O$ and $\delta^{2}H$ values within the unknown observations. Since neither of the *post hoc* correction approaches optimize precision, new strategies for dynamically detecting and accomodating background variation in

N_2, O_2, and/or Ar are needed in order to capitalize on the possibilities of CRDS measurements in variable backgrounds.

Data availability

The data generated in this study are publicly available and can be downloaded from the Open Science Framework (https://doi.org/10.17605/OSF.IO/C7NSG).

Author contributions

J. E. Johnson and C. W. Rella designed the experiments and J. E. Johnson carried them out. Both authors analyzed the results and J. E. Johnson prepared the manuscript with contributions from C. W. Rella.

Competing interests

J. E. Johnson declares no conflict of interest. C. W. Rella is an employee of Picarro, Inc.

Acknowledgements

We are grateful to R. K. Monson (U. of Arizona) for encouragement to pursue these experiments; to J. A. Berry (Carnegie Institution) and C. B. Field (Carnegie Institution) for loaning the Picarro L2120-*i*; to C. Redondo (U. of Arizona), C. Burkhart (Air Liquide), S. Martinez (Air Liquide), and S. Owens (Air Liquide) for assistance obtaining compressed gases; and to D. Dettman (U. of Arizona), F. Dominguez (U. of Illinois), C. Eastoe (U. of Arizona), S. Leavitt (U. of Arizona), and K. Welten (U. of California-Berkeley) for assistance obtaining and calibrating liquid standards. This study was completed with support from the National Science Foundation through the Macrosystem Biology Program Award #1065790 (R.K.M.) and the Major Research Infrastructure Program Award #1040106 (C.B.F. and J.A.B.).

References

Aemisegger, F., Sturm, P., Graf, P., Sodemann, H., Pfahl, S., Knohl, A. and Wernli, H.: Measuring variations of δ^2H and $\delta^{18}O$ in atmospheric water vapour using two commercial laser-based spectrometers: an instrument characterisation study, Atmospheric Measurement Techniques, 5, 1491–1511, doi:10.5194/amt-5-1491-2012, 2012.

Becker, M., Andersen, N., Fiedler, B., Fietzek, P., Körtzinger, A., Steinhoff, T. and Friedrichs, G.: Using cavity ringdown spectroscopy for continuous monitoring of $\delta^{13}C(CO_2)$ and fCO_2 in the surface ocean, Limnol. Oceanogr. Methods, 10, 752–766, doi:10.4319/lom.2012.10.752, 2012.

Berkelhammer, M., Hu, J., Bailey, A., Noone, D., J, S. C., Barnard, H., Gochis, D., Hsiao, G., Rahn, T. and Turnipseed, A.: The nocturnal water cycle in an open-canopy forest, J Geophys Res-Atmos, 118, 10225–10242,

2013.

Brand, W. A., Geilmann, H., Crosson, E. R. and Rella, C. W.: Cavity ring-down spectroscopy versus high-temperature conversion isotope ratio mass spectrometry; a case study on δ^2H and $\delta^{18}O$ of pure water samples and alcohol/water mixtures, Rapid Commun. Mass Spectrom., 23, 1879–1884, doi:10.1002/rcm.4083, 2009.

Brewer, P. J., Brown, R. J. C., Miller, M. N., Miñarro, M. D., Murugan, A., Milton, M. J. T. and Rhoderick, G. C.: Preparation and Validation of Fully Synthetic Standard Gas Mixtures with Atmospheric Isotopic Composition for Global CO 2and CH 4Monitoring, Anal. Chem., 86, 1887–1893, doi:10.1021/ac403982m, 2014.

Buldyreva, J., Lavrentieva, N. and Starikov, V.: Collisional line broadening and shifting of atmospheric gases: a practical guide for line shape modelling by current semi-classical approaches, Imperial College Press, London. 2011.

Casado, M., Landais, A., Masson-Delmotte, V., Genthon, C., Kerstel, E., Kassi, S., Arnaud, L., Picard, G., Prie, F., Cattani, O., Steen-Larsen, H.-C., Vignon, E. and Cermak, P.: Continuous measurements of isotopic composition of water vapour on the East Antarctic Plateau, Atmos Chem Phys, 16, 8521–8538, doi:10.5194/acp-16-8521-2016-supplement, 2016.

Chen, H., Winderlich, J., Gerbig, C., Hoefer, A., Rella, C. W., Crosson, E. R., Van Pelt, A. D., Steinbach, J., Kolle, O., Beck, V., Daube, B. C., Gottlieb, E. W., Chow, V. Y., Santoni, G. W. and Wofsy, S. C.: High-accuracy continuous airborne measurements of greenhouse gases (CO_2 and CH_4) using the cavity ring-down spectroscopy (CRDS) technique, Atmospheric Measurement Techniques, 3, 375:386, 2010.

Crosson, E. R.: A cavity ring-down analyzer for measuring atmospheric levels of methane, carbon dioxide, and water vapor, Appl. Phys. B, 92, 403–408, doi:10.1007/s00340-008-3135-y, 2008.

Demtröder, W.: Laser Spectroscopy 1: Basic Principles, 5 ed., Springer, Berlin. 2014.

Flores, E., Rhoderick, G. C., Viallon, J., Moussay, P., Choteau, T., Gameson, L., Guenther, F. R. and Wielgosz, R. I.: Methane Standards Made in Whole and Synthetic Air Compared by Cavity Ring Down Spectroscopy and Gas Chromatography with Flame Ionization Detection for Atmospheric Monitoring Applications, Anal. Chem., 87, 3272–3279, doi:10.1021/ac5043076, 2015.

Friedrichs, G., Bock, J., Temps, F., Fietzek, P., Körtzinger, A. and Wallace, D. W. R.: Toward continuous monitoring of seawater $^{13}CO_2/^{12}CO_2$ isotope ratio and pCO_2: Performance of cavity ringdown spectroscopy and gas matrix effects, Limnol. Oceanogr. Methods, 8, 539–551, doi:10.4319/lom.2010.8.539, 2010.

Goldenstein, C. S., Miller, V. A., Spearrin, R. M. and Strand, C. L.: SpectraPlot.com: Integrated Spectroscopic Modeling of Atomic and Molecular Gases, Journal of Quantitative Spectroscopy and Radiative Transfer, 1–17, doi:10.1016/j.jqsrt.2017.06.007, 2017.

Goldenstein, C. S., Spearrin, R. M., Jeffries, J. B. and Hanson, R. K.: Infrared laser-absorption sensing for combustion gases, Progress in Energy and Combustion Science, 60, 132–176, doi:10.1016/j.pecs.2016.12.002, 2017.

Goldenstein, C. S., Strand, C. L., Schultz, I. A., Sun, K., Jeffries, J. B. and Hanson, R. K.: Fitting of calibration-free scanned-wavelength-modulation spectroscopy spectra for determination of gas properties and absorption lineshapes, Appl Opt, 53, 356–12, doi:10.1364/AO.53.000356, 2014.

Gralher, B., Herbstritt, B., Weiler, M., Wassenaar, L. I. and Stumpp, C.: Correcting Laser-Based Water Stable Isotope Readings Biased by Carrier Gas Changes, Environ. Sci. Technol., 50, 7074–7081, doi:10.1021/acs.est.6b01124, 2016.

Gupta, P., Noone, D., Galewsky, J., Sweeney, C. and Vaughn, B. H.: Demonstration of high-precision continuous measurements of water vapor isotopologues in laboratory and remote field deployments using wavelength-scanned

cavity ring-down spectroscopy (WS-CRDS) technology, Rapid Commun. Mass Spectrom., 23, 2534–2542, doi:10.1002/rcm.4100, 2009.

Hanson, R. K., Spearrin, R. M. and Goldenstein, C. S.: Spectroscopy and Optical Diagnostics for Gases, Springer, New York. 2015.

Hendry, M. J., Richman, B. and Wassenaar, L. I.: Correcting for Methane Interferences on δ^2H and $\delta^{18}O$ Measurements in Pore Water Using $H_2O_{(liquid)}$–$H_2O_{(vapor)}$ Equilibration Laser Spectroscopy, Anal. Chem., 83, 5789–5796, doi:10.1021/ac201341p, 2011.

Herbstritt, B., Gralher, B. and Weiler, M.: Continuous in situ measurements of stable isotopes in liquid water, Water Resour Res, 48, W03601, doi:10.1029/2011WR011369, 2012.

Hodges, J. T. and Lisak, D.: Frequency-stabilized cavity ring-down spectrometer for high-sensitivity measurements of water vapor concentration, Appl. Phys. B, 85, 375–382, doi:10.1007/s00340-006-2411-y, 2006.

Johnson, J. E., Hamann, L., Dettman, D. L., Kim-Hak, D., Leavitt, S. W., Monson, R. K. and Papuga, S. A.: Performance of induction module-cavity ring-down spectroscopy (IM-CRDS) for measuring $\delta^{18}O$ and δ^2H values of soil, stem, and leaf waters, Rapid Commun. Mass Spectrom., 31, 547–560, doi:10.1002/rcm.7813, 2017.

Larsen, M., Lehner, P., Borisov, S. M., Klimant, I., Fischer, J. P., Stewart, F. J., Canfield, D. E. and Glud, R. N.: In situ quantification of ultra-low O_2 concentrations in oxygen minimum zones: Application of novel optodes, Limnol. Oceanogr. Methods, 14, 784–800, doi:10.1002/lom3.10126, 2016.

Lazarus, B. E., Germino, M. J. and Vander Veen, J. L.: Online induction heating for determination of isotope composition of woody stem water with laser spectrometry: a methods assessment, Isotopes in Environmental and Health Studies, 52, 309–325, doi:10.1080/10256016.2016.1141205, 2016.

Lisak, D., Havey, D. K. and Hodges, J. T.: Spectroscopic line parameters of water vapor for rotation-vibration transitions near 7180 cm^{-1}, Phys. Rev. A, 79(5), 052507, doi:10.1103/PhysRevA.79.052507, 2009.

Long, D. A., Gameson, L., Truong, G. W., Bielska, K., Cygan, A., Hodges, J. T., Whetstone, J. R. and van Zee, R. D.: The Effects of Variations in Buffer Gas Mixing Ratios on Commercial Carbon Dioxide Cavity Ring-Down Spectroscopy Sensors, J. Atmos. Oceanic Technol., 30, 2604–2609, doi:10.1175/JTECH-D-13-00039.1, 2013.

Martín-Gómez, P., Barbeta, A., Voltas, J., Penuelas, J., Dennis, K., Palacio, S., Dawson, T. E. and Ferrio, J. P.: Isotope-ratio infrared spectroscopy: a reliable tool for the investigation of plant-water sources? New Phytologist, 207, 914–927, doi:10.1111/nph.13376, 2015.

Munksgaard, N. C., Wurster, C. M. and Bird, M. I.: Continuous analysis of $\delta^{18}O$ and δD values of water by diffusion sampling cavity ring-down spectrometry: a novel sampling device for unattended field monitoring of precipitation, ground and surface waters, Rapid Commun. Mass Spectrom., 25, 3706–3712, doi:10.1002/rcm.5282, 2011.

Munksgaard, N. C., Wurster, C. M., Bass, A., Zagorskis, I. and Bird, M. I.: First continuous shipboard $\delta^{18}O$ and δD measurements in sea water by diffusion sampling—cavity ring-down spectrometry, Environ Chem Lett, 10, 301–307, doi:10.1007/s10311-012-0371-5, 2012.

Nara, H., Tanimoto, H., Tohjima, Y., Mukai, H., Nojiri, Y., Katsumata, K. and Rella, C. W.: Effect of air composition (N_2, O_2, Ar, and H_2O) on CO_2 and CH_4 measurement by wavelength-scanned cavity ring-down spectroscopy: calibration and measurement strategy, Atmospheric Measurement Techniques, 5, 2689–2701, doi:10.5194/amt-5-2689-2012, 2012.

O'Boyle, S., McDermott, G., Silke, J. and Cusack, C.: Potential impact of an exceptional bloom of *Karenia mikimotoi* on dissolved oxygen levels in waters off western Ireland, Harmful Algae, 53, 77–85, doi:10.1016/j.hal.2015.11.014, 2016.

O'Keefe, A. and Deacon, D.: Cavity ring-down optical spectrometer for absorption measurements using pulsed laser sources, Review of Scientific Instruments, 59, 2544–2551, doi:10.1063/1.1139895, 1988.

R Core Team. R: A language and environment for statistical computing, R Foundation for Statistical Computing, Vienna, Austria. Available from: http://www.R-project.org/, 2016.

Rella, C. W.: Accurate Greenhouse Gas Measurements in Humid Gas Streams Using the Picarro G1301 Carbon Dioxide / Methane / Water Vapor Gas Analyzer, 1–18. Available from: https://www.picarro.com/assets/docs/White_Paper_G1301_Water_Vapor_Correction.pdf, 2010.

Rella, C. W., Hoffnagle, J., He, Y. and Tajima, S.: Local- and regional-scale measurements of CH_4, $\delta^{13}CH_4$, and C_2H_6 in the Uintah Basin using a mobile stable isotope analyzer, Atmospheric Measurement Techniques, 8, 4539–4559, doi:10.5194/amt-8-4539-2015, 2015.

Schmidt, M. and Eggert, A.: Oxygen cycling in the northern Benguela Upwelling System: Modelling oxygen sources and sinks, Progress in Oceanography, 149, 145–173, doi:10.1016/j.pocean.2016.09.004, 2016.

Schmidt, M., Maseyk, K., Lett, C., Biron, P., Richard, P., Bariac, T. and Seibt, U.: Concentration effects on laser-based $\delta^{18}O$ and $\delta^{2}H$ measurements and implications for the calibration of vapour measurements with liquid standards, Rapid Commun. Mass Spectrom., 24, 3553–3561, doi:10.1002/rcm.4813, 2010.

Schmidt, M., Maseyk, K., Lett, C., Biron, P., Richard, P., Bariac, T. and Seibt, U.: Reducing and correcting for contamination of ecosystem water stable isotopes measured by isotope ratio infrared spectroscopy, Rapid Commun. Mass Spectrom., 26, 141–153, doi:10.1002/rcm.5317, 2012.

Schultz, N. M., Griffis, T. J., Lee, X. and Baker, J. M.: Identification and correction of spectral contamination in $^{2}H/^{1}H$ and $^{18}O/^{16}O$ measured in leaf, stem, and soil water, Rapid Commun. Mass Spectrom., 25, 3360–3368, doi:10.1002/rcm.5236, 2011.

Sprenger, M., Tetzlaff, D. and Soulsby, C.: No influence of CO_2 on stable isotope analyses of soil waters with OA-ICOS, Rapid Commun. Mass Spectrom., 31, 430-436, doi:10.1002/rcm.7815, 2017.

Steen-Larsen, H. C., Sveinbjörnsdóttir, A. E., Peters, A. J., Masson-Delmotte, V., Guishard, M. P., Hsiao, G., Jouzel, J., Noone, D., Warren, J. K. and White, J. W. C.: Climatic controls on water vapor deuterium excess in the marine boundary layer of the North Atlantic based on 500 days of in situ, continuous measurements, Atmos. Chem. Phys. Discuss., 14, 2363–2401, doi:10.5194/acpd-14-2363-2014, 2014.

Steig, E. J., Gkinis, V., Schauer, A. J., Schoenemann, S. W., Samek, K., Hoffnagle, J., Dennis, K. J. and Tan, S. M.: Calibrated high-precision ^{17}O-excess measurements using cavity ring-down spectroscopy with laser-current-tuned cavity resonance, Atmospheric Measurement Techniques, 7, 2421–2435, doi:10.5194/amt-7-2421-2014, 2014.

Sun, K., Chao, X., Sur, R., Goldenstein, C. S., Jeffries, J. B. and Hanson, R. K.: Analysis of calibration-free wavelength-scanned wavelength modulation spectroscopy for practical gas sensing using tunable diode lasers, Meas. Sci. Technol., 24, 125203–12, doi:10.1088/0957-0233/24/12/125203, 2013.

Sur, R., Sun, K., Jeffries, J. B., Socha, J. G. and Hanson, R. K.: Scanned-wavelength-modulation-spectroscopy sensor for CO, CO_2, CH_4 and H_2O in a high-pressure engineering-scale transport-reactor coal gasifier, Fuel, 150, 102–111, doi:10.1016/j.fuel.2015.02.003, 2015.

Tennyson, J., Bernath, P. F., Brown, L. R., Campargue, A., Carleer, M. R., Császár, A. G., Gamache, R. R., Hodges, J. T., Jenouvrier, A., Naumenko, O. V., Polyansky, O. L., Rothman, L. S., Toth, R. A., Vandaele, A. C., Zobov, N. F., Daumont, L., Fazliev, A. Z., Furtenbacher, T., Gordon, I. E., Mikhailenko, S. N. and Shirin, S. V.: IUPAC critical evaluation of the rotational–vibrational spectra of water vapor. Part I—Energy levels and transition wavenumbers for $H_2{}^{17}O$ and $H_2{}^{18}O$, Journal of Quantitative Spectroscopy and Radiative Transfer, 110, 573–596, doi:10.1016/j.jqsrt.2009.02.014, 2009.

Tennyson, J., Bernath, P. F., Brown, L. R., Campargue, A., Császár, A. G., Daumont, L., Gamache, R. R., Hodges, J. T., Naumenko, O. V., Polyansky, O. L., Rothman, L. S., Toth, R. A., Vandaele, A. C., Zobov, N. F., Fally, S., Fazliev, A. Z., Furtenbacher, T., Gordon, I. E., Hu, S.-M., Mikhailenko, S. N. and Voronin, B. A.: IUPAC critical evaluation of the rotational–vibrational spectra of water vapor. Part II Energy levels and transition wavenumbers for $HD^{16}O$, $HD^{17}O$, and $HD^{18}O$, Journal of Quantitative Spectroscopy and Radiative Transfer, 111, 2160–2184, doi:10.1016/j.jqsrt.2010.06.012, 2010.

Tennyson, J., Bernath, P. F., Brown, L. R., Campargue, A., Császár, A. G., Daumont, L., Gamache, R. R., Hodges, J. T., Naumenko, O. V., Polyansky, O. L., Rothman, L. S., Vandaele, A. C., Zobov, N. F., Derzi, Al, A. R., Fábri, C., Fazliev, A. Z., Furtenbacher, T., Gordon, I. E., Lodi, L. and Mizus, I. I.: IUPAC critical evaluation of the rotational–vibrational spectra of water vapor, Part III: Energy levels and transition wavenumbers for $H_2{}^{16}O$, Journal of Quantitative Spectroscopy and Radiative Transfer, 117, 29–58, doi:10.1016/j.jqsrt.2012.10.002, 2013.

Volkmann, T. H. M. and Weiler, M.: Continual in situ monitoring of pore water stable isotopes in the subsurface, Hydrol. Earth Syst. Sci., 18, 1819–1833, doi:10.5194/hess-18-1819-2014, 2014.

West, A. G., Goldsmith, G. R., Brooks, P. D. and Dawson, T. E.: Discrepancies between isotope ratio infrared spectroscopy and isotope ratio mass spectrometry for the stable isotope analysis of plant and soil waters, Rapid Commun. Mass Spectrom., 24, 1948–1954, doi:10.1002/rcm.4597, 2010.

West, A. G., Goldsmith, G. R., Matimati, I. and Dawson, T. E.: Spectral analysis software improves confidence in plant and soil water stable isotope analyses performed by isotope ratio infrared spectroscopy (IRIS), Rapid Commun. Mass Spectrom., 25, 2268–2274, doi:10.1002/rcm.5126, 2011.

Zalicki, P. and Zare, R. N.: Cavity ring-down spectroscopy for quantitative absorption measurements, The Journal of Chemical Physics, 102, 2708–2717, 1995.

List of Figures

Figure 1. Schematic diagram of the mixing system used for the experiments. Pure background gases were obtained commercially, mixed with mass flow controllers, and supplied to the inlet of the L2120-*i* at a slight overpressure. See text for details.

Figure 2. Sensitivity of $\delta^{18}O$ and $\delta^{2}H$ values to background N_2, O_2, and Ar mixing ratios. For each experiment, sensitivity is plotted as the difference between the apparent and true isotopic composition of the standards (i.e., $\Delta\delta^{18}O = \delta^{18}O_{apparent} - \delta^{18}O_{true}$ and $\Delta\delta^{2}H = \delta^{2}H_{apparent} - \delta^{2}H_{true}$). For each panel, n = 330 measurements of four liquid standards across a range of injection volumes (i.e., 400-2400 nL, in eleven steps of 200 nL each). Points represent mean values ± s.d. for replicates of each standard at each injection volume, and regression slopes are given by β_5 values in Table 2.

Figure 3. Relationship between the spectral residuals, $\Delta\delta^{18}O$, and $\Delta\delta^{2}H$ values. For each panel, n = 330 measurements of four liquid standards across a range of injection volumes (i.e., 400-2400 nL, in eleven steps of 200 nL each). Points represent mean values ± s.d. for replicates of each standard at each injection volume.

Figure 4. Relationship between the spectral baseline, $\Delta\delta^{18}O$, and $\Delta\delta^{2}H$ values. For each panel, n = 330 measurements of four liquid standards across a range of injection volumes (i.e., 400-2400 nL, in eleven steps of 200 nL each). Points represent mean values ± s.d. for replicates of each standard at each injection volume.

Figure 5. Relationship between the baseline slope, $\Delta\delta^{18}O$, and $\Delta\delta^{2}H$ values. For each panel, n = 330 measurements of four liquid standards across a range of injection volumes (i.e., 400-2400 nL, in eleven steps of 200 nL each). Points represent mean values ± s.d. for replicates of each standard at each injection volume.

Figure 6. Relationship between the frequency shift, $\Delta\delta^{18}O$, and $\Delta\delta^{2}H$ values. For each panel, n = 330 measurements of four liquid standards across a range of injection volumes (i.e., 400-2400 nL, in eleven steps of 200 nL each). Points represent mean values ± s.d. for replicates of each standard at each injection volume.

Figure 7. Relationship between the frequency scale correction, $\Delta\delta^{18}O$, and $\Delta\delta^{2}H$ values. For each panel, n = 330 measurements of four liquid standards across a range of injection volumes (i.e., 400-2400 nL, in eleven steps of 200 nL each). Points represent mean values ± s.d. for replicates of each standard at each injection volume.

Figure 8. Relationship between the fixed linewidth parameter, $\Delta\delta^{18}O$, and $\Delta\delta^{2}H$ values. For each panel, n = 330 measurements of four liquid standards across a range of injection volumes (i.e., 400-2400 nL, in eleven

steps of 200 nL each). Points represent mean values ± s.d. for replicates of each standard at each injection volume.

Figure 9. Relationship between the free linewidth parameter, $\Delta\delta^{18}O$, and $\Delta\delta^{2}H$ values. For each panel, n = 330 measurements of four liquid standards across a range of injection volumes (i.e., 400-2400 nL, in eleven steps of 200 nL each). Points represent mean values ± s.d. for replicates of each standard at each injection volume.

Figure 10. Relationships between H_2O mixing ratio and the spectral residuals, baseline, and baseline slope parameters. For each panel, n = 990 measurements of four liquid standards across a range of injection volumes (i.e., 400-2400 nL, in eleven steps of 200 nL each). Points represent mean values ± s.d. for replicates of each standard at each injection volume.

Figure 11. Relationships between H_2O mixing ratio and the frequency shift, frequency scale correction, fixed linewidth, and free linewidth parameters. For each panel, n = 990 measurements of four liquid standards across a range of injection volumes (i.e., 400-2400 nL, in eleven steps of 200 nL each). Points represent mean values ± s.d. for replicates of each standard at each injection volume.

Figure 12. Direct and indirect effects of background gas composition on peak amplitude determination. Panels (a) and (b) plot theoretical spectrograms illustrating how isolated absorption features are directly broadened by air (solid line) versus N_2 (dashed line) or O_2 and Ar (dotted line). Panel (c) plots simulated spectrograms illustrating how the baseline of the three H_2O lines targeted by the L2120-*i* is indirectly affected by the strong neighboring lines at lower frequencies. Simulations were performed using spectraplot.com (Goldenstein et al. 2017) with HITRAN/HITEMP data and the following parameters: T = 80°C, P = 35 torr, and L = 1 cm. The thick line is a simulation at 2.5 % H_2O, and the thin line is a simulation at 0.5 % H_2O.

Figure 1. Schematic diagram of the mixing system used for the experiments. Pure background gases were obtained commercially, mixed with mass flow controllers, and supplied to the inlet of the L2120-*i* at a slight overpressure. See text for details.

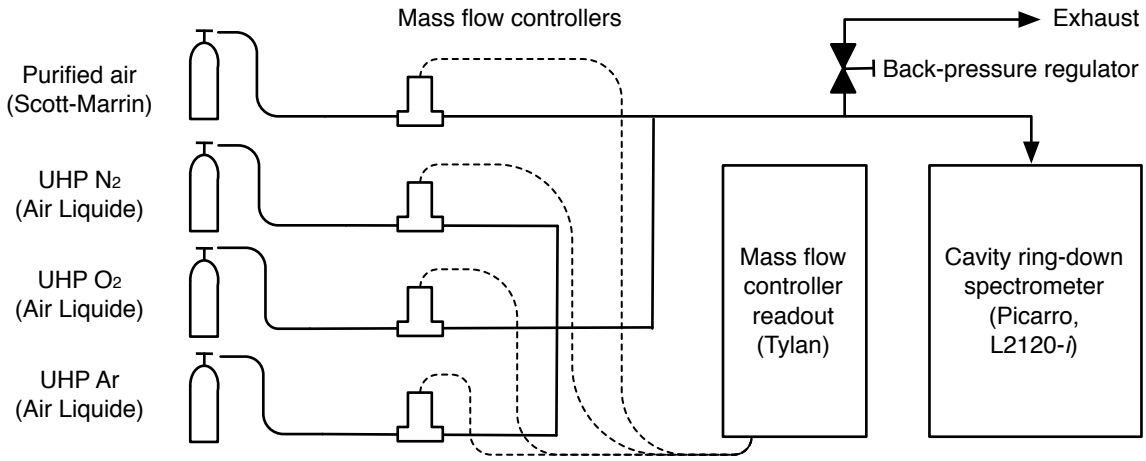

Figure 2. Sensitivity of $\delta^{18}O$ and $\delta^{2}H$ values to background N_2, O_2, and Ar mixing ratios. For each experiment, sensitivity is plotted as the difference between the apparent and true isotopic composition of the standards (i.e., $\Delta\delta^{18}O = \delta^{18}O_{apparent} - \delta^{18}O_{true}$ and $\Delta\delta^{2}H = \delta^{2}H_{apparent} - \delta^{2}H_{true}$). For each panel, n = 330 measurements of four liquid standards across a range of injection volumes (i.e., 400-2400 nL, in eleven steps of 200 nL each). Points represent mean values ± s.d. for replicates of each standard at each injection volume, and regression slopes are given by β_5 values in Table 2.

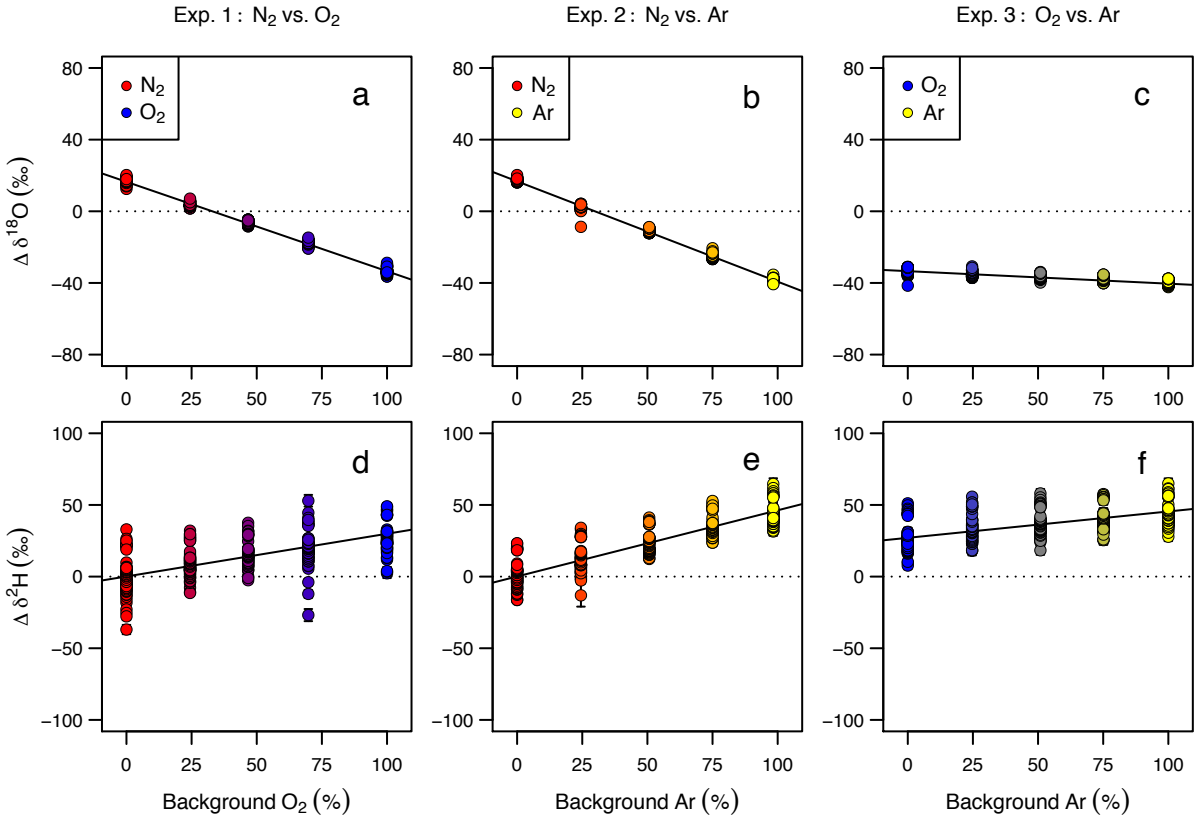

Figure 3. Relationship between the spectral residuals, $\Delta\delta^{18}O$, and $\Delta\delta^{2}H$ values. For each panel, n = 330 measurements of four liquid standards across a range of injection volumes (i.e., 400-2400 nL, in eleven steps of 200 nL each). Points represent mean values ± s.d. for replicates of each standard at each injection volume.

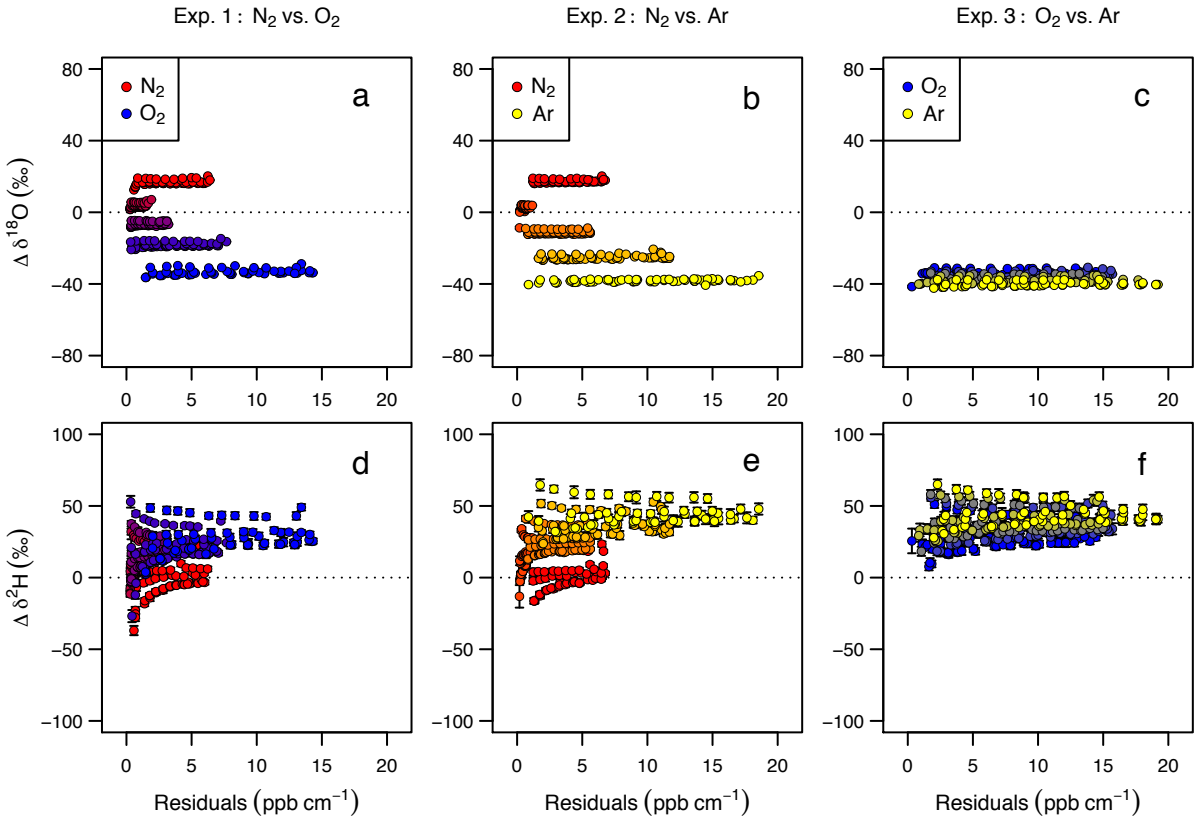

Figure 4. Relationship between the spectral baseline, $\Delta\delta^{18}O$, and $\Delta\delta^{2}H$ values. For each panel, n = 330 measurements of four liquid standards across a range of injection volumes (i.e., 400-2400 nL, in eleven steps of 200 nL each). Points represent mean values ± s.d. for replicates of each standard at each injection volume.

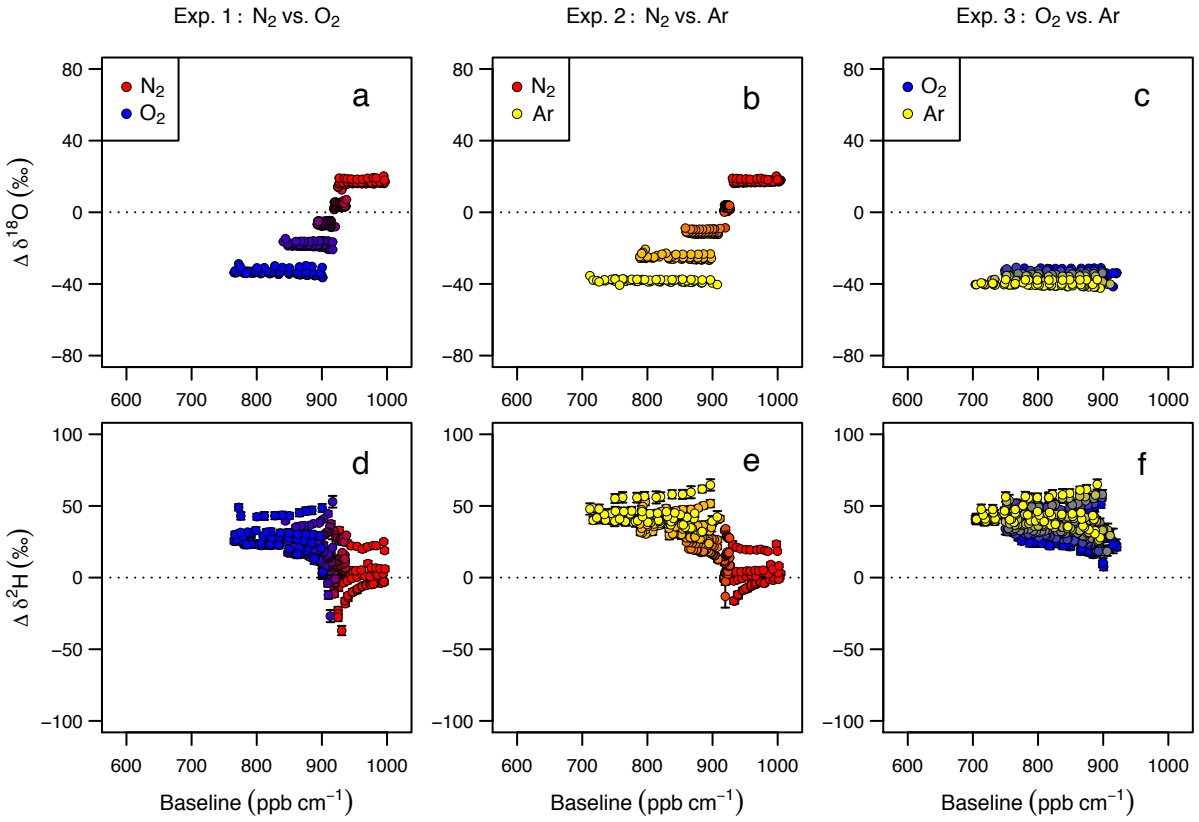

Figure 5. Relationship between the baseline slope, $\Delta\delta^{18}O$, and $\Delta\delta^{2}H$ values. For each panel, n = 330 measurements of four liquid standards across a range of injection volumes (i.e., 400-2400 nL, in eleven steps of 200 nL each). Points represent mean values ± s.d. for replicates of each standard at each injection volume.

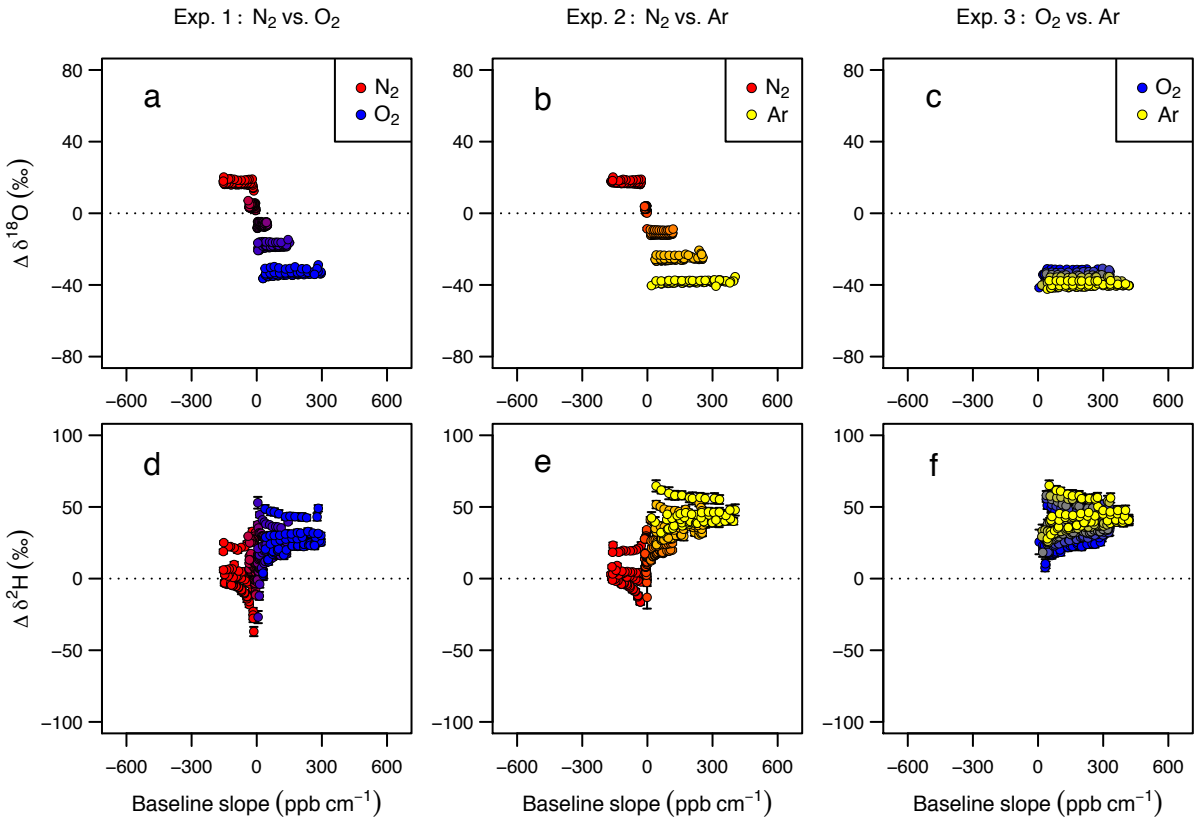

Figure 6. Relationship between the frequency shift, $\Delta\delta^{18}O$, and $\Delta\delta^{2}H$ values. For each panel, n = 330 measurements of four liquid standards across a range of injection volumes (i.e., 400-2400 nL, in eleven steps of 200 nL each). Points represent mean values ± s.d. for replicates of each standard at each injection volume.

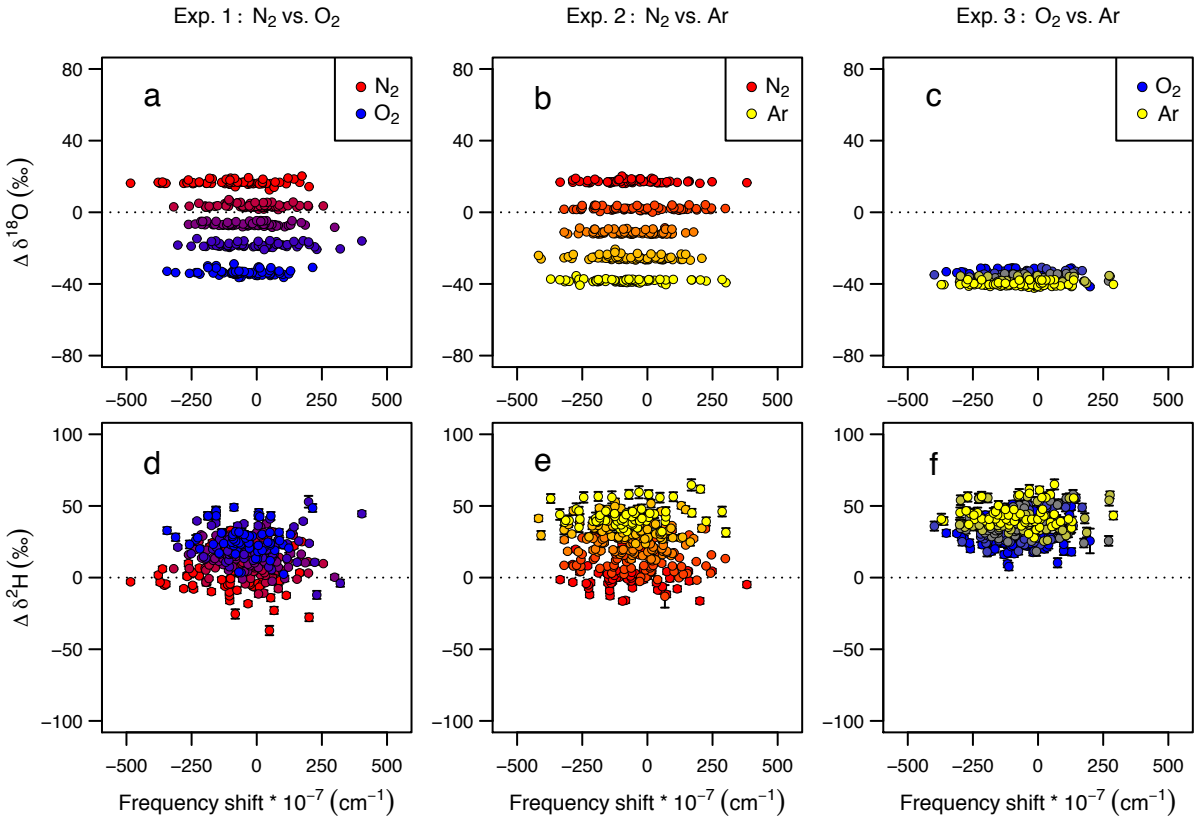

Figure 7. Relationship between the frequency scale correction, $\Delta\delta^{18}O$, and $\Delta\delta^{2}H$ values. For each panel, n = 330 measurements of four liquid standards across a range of injection volumes (i.e., 400-2400 nL, in eleven steps of 200 nL each). Points represent mean values ± s.d. for replicates of each standard at each injection volume.

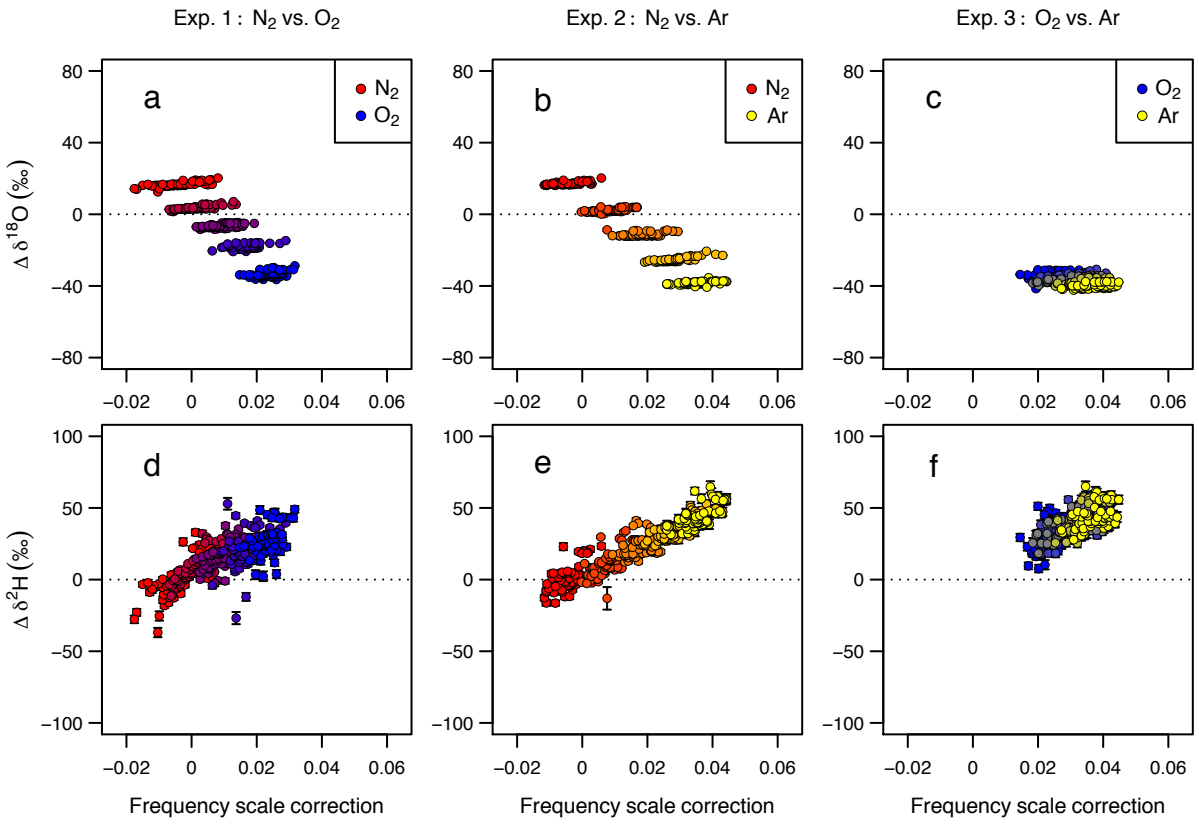

Figure 8. Relationship between the fixed linewidth parameter, $\Delta\delta^{18}O$, and $\Delta\delta^{2}H$ values. For each panel, n = 330 measurements of four liquid standards across a range of injection volumes (i.e., 400-2400 nL, in eleven steps of 200 nL each). Points represent mean values ± s.d. for replicates of each standard at each injection volume.

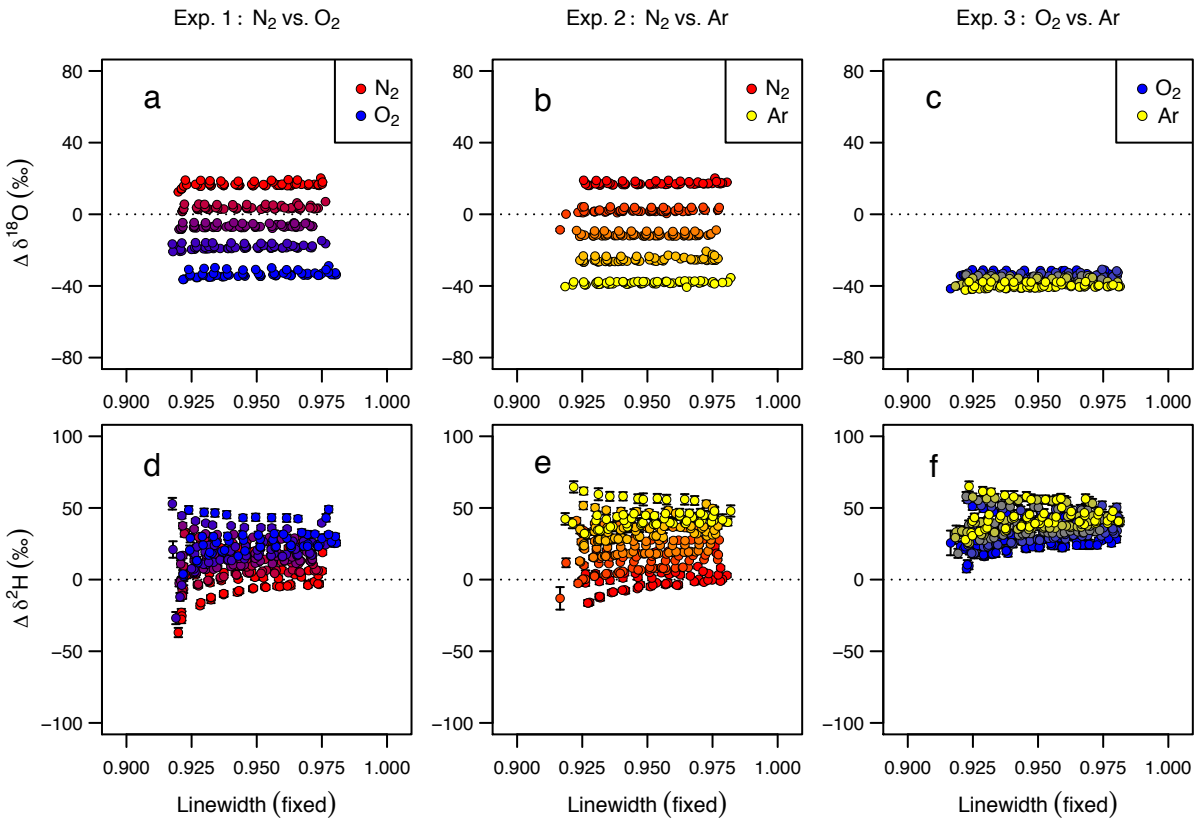

Figure 9. Relationship between the free linewidth parameter, $\Delta\delta^{18}O$, and $\Delta\delta^{2}H$ values. For each panel, n = 330 measurements of four liquid standards across a range of injection volumes (i.e., 400-2400 nL, in eleven steps of 200 nL each). Points represent mean values ± s.d. for replicates of each standard at each injection volume.

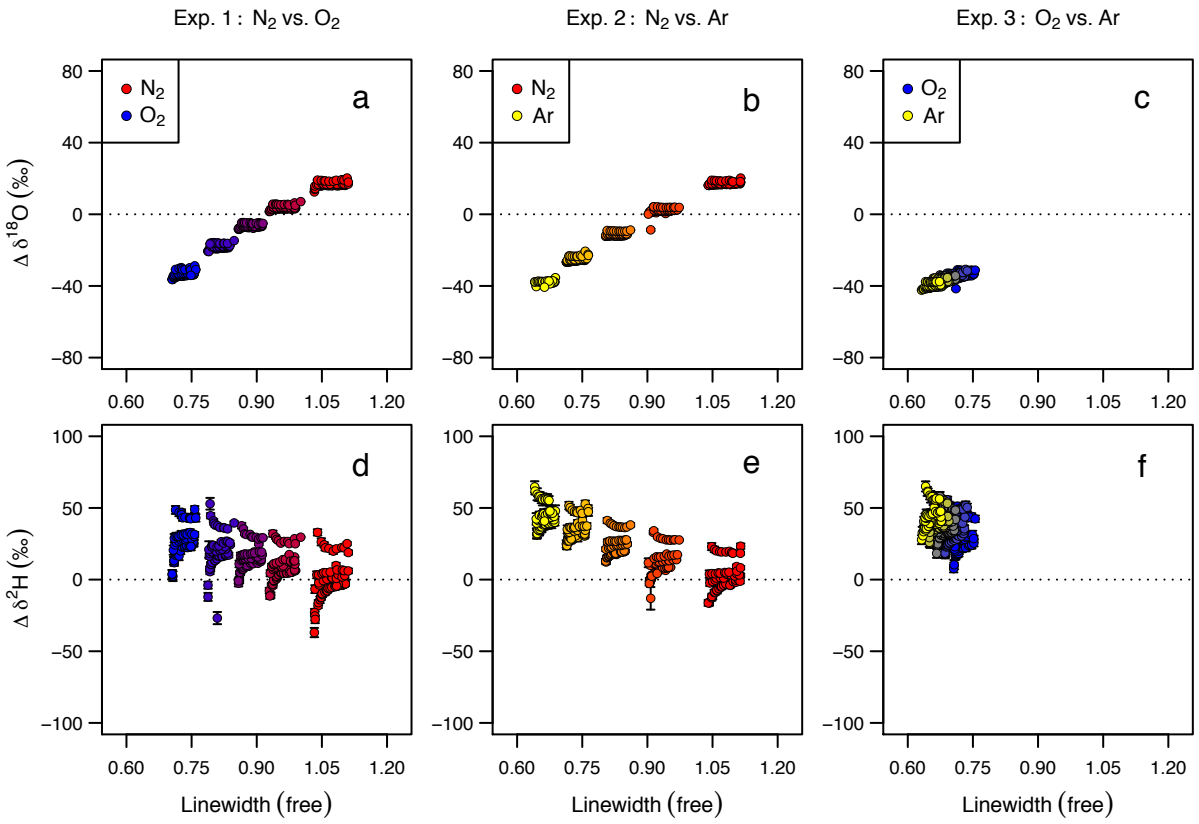

Figure 10. Relationships between H_2O mixing ratio and the spectral residuals, baseline, and baseline slope parameters. For each panel, n = 990 measurements of four liquid standards across a range of injection volumes (i.e., 400-2400 nL, in eleven steps of 200 nL each). Points represent mean values ± s.d. for replicates of each standard at each injection volume.

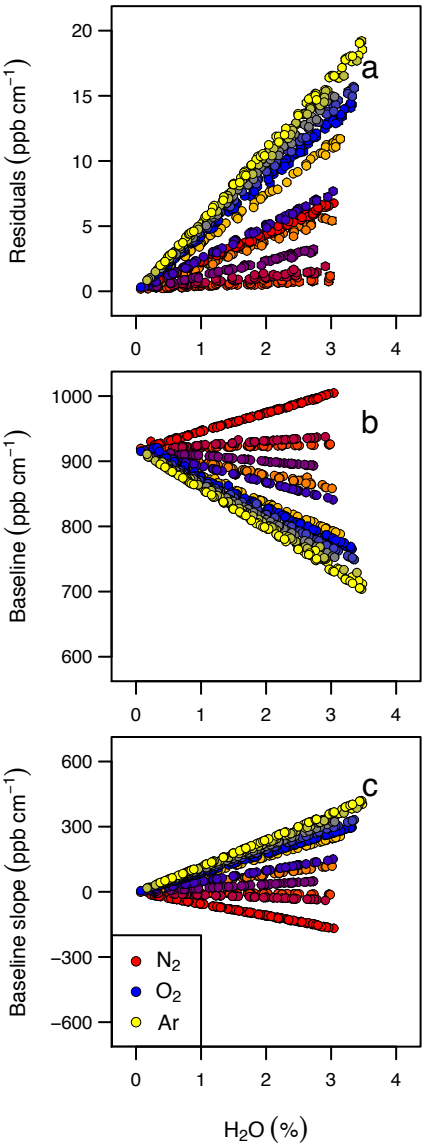

Figure 11. Relationships between H_2O mixing ratio and the frequency shift, frequency scale correction, fixed linewidth, and free linewidth parameters. For each panel, n = 990 measurements of four liquid standards across a range of injection volumes (i.e., 400-2400 nL, in eleven steps of 200 nL each). Points represent mean values ± s.d. for replicates of each standard at each injection volume.

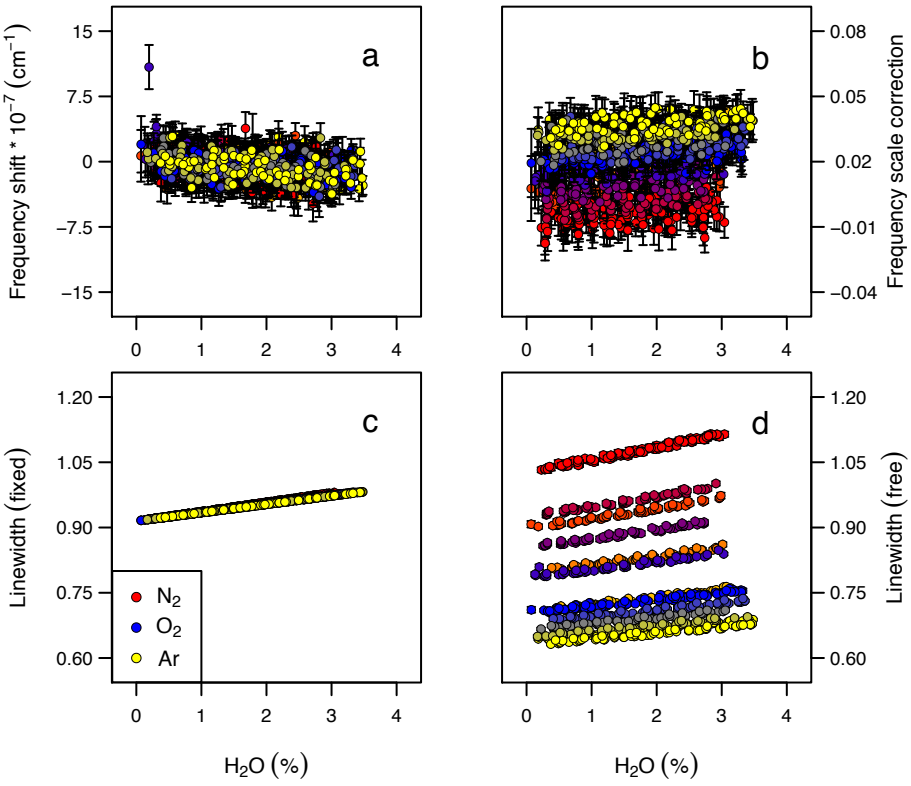

Figure 12. Direct and indirect effects of background gas composition on peak amplitude determination. Panels (a) and (b) plot theoretical spectrograms illustrating how isolated absorption features are directly broadened by air (solid line) versus N_2 (dashed line) or O_2 and Ar (dotted line). Panel (c) plots simulated spectrograms illustrating how the baseline of the three H_2O lines targeted by the L2120-*i* is indirectly affected by the strong neighboring lines at lower frequencies. Simulations were performed using spectraplot.com (Goldenstein et al. 2017) with HITRAN/HITEMP data and the following parameters: T = 80°C, P = 35 torr, and L = 1 cm. The thick line is a simulation at 2.5 % H_2O, and the thin line is a simulation at 0.5 % H_2O.

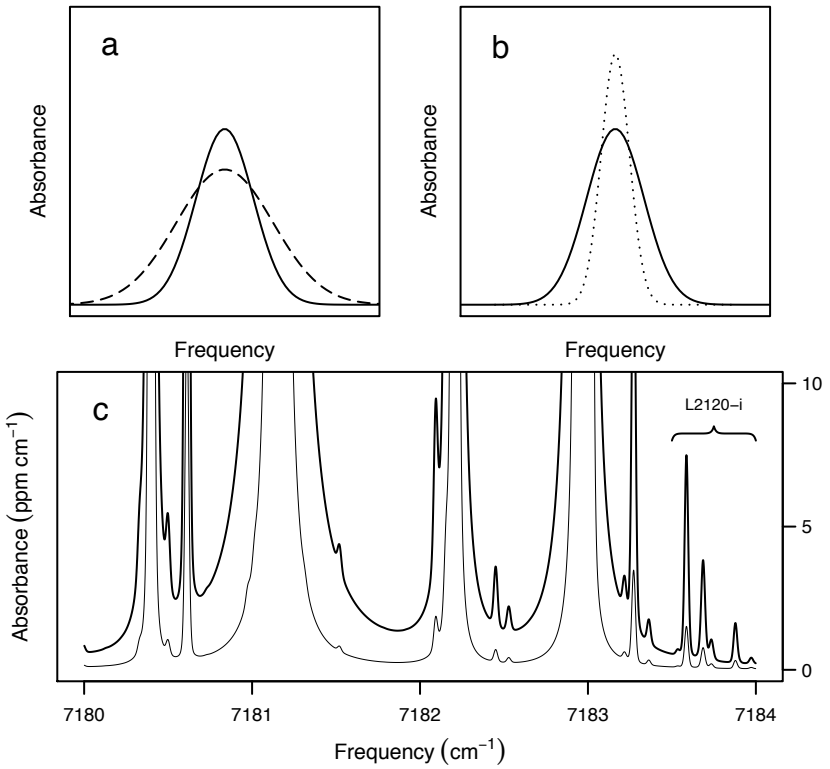

List of Tables

Table 1. Empirical models of the sensitivity of $\delta^{18}O$ and $\delta^{2}H$ values to H_2O in pure N_2, O_2, and Ar. For significant predictors, coefficient estimates are given for β_2, β_3, and β_4 in Eq. 3 (see text). Overall model fit is summarized with the residual standard error (RSE), adjusted R^2 and P-value. Abbreviation: n.s., not significant.

Table 2. Empirical models of the sensitivity of $\delta^{18}O$ and $\delta^{2}H$ values to each of the binary mixtures of N_2, O_2, and Ar. For significant predictors, coefficient estimates are given for β_5 in Eq. 4 (see text). Overall model fit is summarized with the residual standard error (RSE), adjusted R^2 and P-value.

Table 3. Empirical models of the composite sensitivity of $\delta^{18}O$ and $\delta^{2}H$ values to all of the binary mixtures of N_2, O_2, and Ar. For significant predictors, coefficient estimates are given for β_5 and β_6 in Eq. 5 (see text). Overall model fit is summarized with the residual standard error (RSE), adjusted R^2 and P-value.

Table 4. Semi-mechanistic models of the composite sensitivity of $\delta^{18}O$ and $\delta^{2}H$ values to all of the binary mixtures of N_2, O_2, and Ar. For significant predictors, coefficient estimates are given for β_7 and β_8 in Eq. 6 (see text). Overall model fit is summarized with the residual standard error (RSE), adjusted R^2 and P-value.

Table 5. Comparison of empirical and semi-mechanistic models for predicting $\delta^{18}O$ and $\delta^{2}H$ values in a ternary mixture of N_2, O_2, and Ar. Overall model fit is summarized with the residual standard error (RSE), adjusted R^2 and P-value.

Table 1. Empirical models of the sensitivity of $\delta^{18}O$ and $\delta^{2}H$ values to H_2O in pure N_2, O_2, and Ar. For significant predictors, coefficient estimates are given for β_2, β_3, and β_4 in Eq. 3 (see text). Overall model fit is summarized with the residual standard error (RSE), adjusted R^2 and P-value. Abbreviation: n.s., not significant.

Model	Background	n	Response & Predictor	Mean ± SE (‰ ppm^{-1})	RSE (‰)	Adj. R^2	P-value
1	N_2	132	$\partial(\delta^{18}O_{app})\ \partial(H_2O)^{-1}$	-2.7e-04 ± 4.7e-05	-	-	-
			$\partial(\delta^{18}O_{app})\ \partial(1/H_2O)^{-1}$	-1.3e+04 ± 1.5e+03	-	-	-
			$\partial(\delta^{18}O_{app})\ \partial(H_2O^2)^{-1}$	6.4e-09 ± 1.2e-09	-	-	-
			-	-	0.44	0.997	< 0.001
2	N_2	132	$\partial(\delta^{2}H_{app})\ \partial(H_2O)^{-1}$	n.s.	-	-	-
			$\partial(\delta^{2}H_{app})\ \partial(1/H_2O)^{-1}$	-6.9e+04 ± 1.2e+04	-	-	-
			$\partial(\delta^{2}H_{app})\ \partial(H_2O^2)^{-1}$	2.0e-08 ± 9.5e-09	-	-	-
			-	-	3.66	0.998	< 0.001
3	O_2	132	$\partial(\delta^{18}O_{app})\ \partial(H_2O)^{-1}$	-9.2e-05 ± 2.0e-05	-	-	-
			$\partial(\delta^{18}O_{app})\ \partial(1/H_2O)^{-1}$	-6.9e+03 ± 3.5e+02	-	-	-
			$\partial(\delta^{18}O_{app})\ \partial(H_2O^2)^{-1}$	2.9e-09 ± 5.2e-10	-	-	-
			-	-	0.37	0.998	< 0.001
4	O_2	132	$\partial(\delta^{2}H_{app})\ \partial(H_2O)^{-1}$	9.0e-04 ± 1.8e-04	-	-	-
			$\partial(\delta^{2}H_{app})\ \partial(1/H_2O)^{-1}$	n.s.	-	-	-
			$\partial(\delta^{2}H_{app})\ \partial(H_2O^2)^{-1}$	-1.6e-08 ± 4.6e-09	-	-	-
			-	-	3.28	0.998	< 0.001
5	Ar	132	$\partial(\delta^{18}O_{app})\ \partial(H_2O)^{-1}$	n.s.	-	-	-
			$\partial(\delta^{18}O_{app})\ \partial(1/H_2O)^{-1}$	n.s.	-	-	-
			$\partial(\delta^{18}O_{app})\ \partial(H_2O^2)^{-1}$	n.s.	-	-	-
			-	-	1.16	0.983	< 0.001
6	Ar	132	$\partial(\delta^{2}H_{app})\ \partial(H_2O)^{-1}$	n.s.	-	-	-
			$\partial(\delta^{2}H_{app})\ \partial(1/H_2O)^{-1}$	n.s.	-	-	-
			$\partial(\delta^{2}H_{app})\ \partial(H_2O^2)^{-1}$	n.s.	-	-	-
			-	-	2.29	0.999	< 0.001

Table 2. Empirical models of the sensitivity of $\delta^{18}O$ and $\delta^{2}H$ values to each of the binary mixtures of N_2, O_2, and Ar. For significant predictors, coefficient estimates are given for β_5 in Eq. 4 (see text). Overall model fit is summarized with the residual standard error (RSE), adjusted R^2 and P-value.

Model	Background	n	Response & Predictor	Mean ± SE (‰ $\%^{-1}$)	RSE (‰)	Adj. R^2	P-value
1	N_2, O_2	330	$\partial(\delta^{18}O_{app})\ \partial(O_2)^{-1}$	-0.50 ± 0.001	0.62	0.999	< 0.001
2	N_2, O_2	330	$\partial(\delta^{2}H_{app})\ \partial(O_2)^{-1}$	0.26 ± 0.009	5.19	0.995	< 0.001
3	N_2, Ar	330	$\partial(\delta^{18}O_{app})\ \partial(Ar)^{-1}$	-0.56 ± 0.001	0.62	0.999	< 0.001
4	N_2, Ar	330	$\partial(\delta^{2}H_{app})\ \partial(Ar)^{-1}$	0.43 ± 0.005	3.16	0.998	< 0.001
5	O_2, Ar	330	$\partial(\delta^{18}O_{app})\ \partial(Ar)^{-1}$	-0.06 ± 0.001	0.33	0.999	< 0.001
6	O_2, Ar	330	$\partial(\delta^{2}H_{app})\ \partial(Ar)^{-1}$	0.15 ± 0.005	3.33	0.998	< 0.001

Table 3. Empirical models of the composite sensitivity of $\delta^{18}O$ and $\delta^{2}H$ values to all of the binary mixtures of N_2, O_2, and Ar. For significant predictors, coefficient estimates are given for β_5 and β_6 in Eq. 5 (see text). Overall model fit is summarized with the residual standard error (RSE), adjusted R^2 and P-value.

Model	**Background**	**n**	**Response & Predictor**	**Mean ± SE** (‰ $\%^{-1}$)	**RSE** (‰)	**Adj. R^2**	**P-value**
1	N_2, O_2, Ar	990	$\partial(\delta^{18}O_{app})\ \partial(O_2)^{-1}$	-0.50 ± 0.001	-	-	-
			$\partial(\delta^{18}O_{app})\ \partial(Ar)^{-1}$	-0.57 ± 0.001	-	-	-
			-	-	0.62	0.999	< 0.001
2	N_2, O_2, Ar	990	$\partial(\delta^{2}H_{app})\ \partial(O_2)^{-1}$	0.26 ± 0.004	-	-	-
			$\partial(\delta^{2}H_{app})\ \partial(Ar)^{-1}$	0.42 ± 0.004	-	-	-
			-	-	3.59	0.998	< 0.001

Table 4. Semi-mechanistic models of the composite sensitivity of $\delta^{18}O$ and $\delta^{2}H$ values to all of the binary mixtures of N_2, O_2, and Ar. For significant predictors, coefficient estimates are given for β_7 in Eq. 6 (see text). Overall model fit is summarized with the residual standard error (RSE), adjusted R^2 and P-value.

Model	Background	n	Response & Predictor	Mean ± SE (‰ unit^{-1})	RSE (‰)	Adj. R^2	P-value
1	N_2, O_2, Ar	990	$\partial(\delta^{18}O_{app})$ ∂(frequency shift)$^{-1}$	n.s.	19.88	0.164	< 0.001
2	N_2, O_2, Ar	990	$\partial(\delta^{18}O_{app})$ ∂(residuals)$^{-1}$	-5.0 ± 1.3e-01	12.80	0.653	< 0.001
3	N_2, O_2, Ar	990	$\partial(\delta^{18}O_{app})$ ∂(fixed linewidth)$^{-1}$	1.2e04 ± 2.0e02	9.20	0.821	< 0.001
4	N_2, O_2, Ar	990	$\partial(\delta^{18}O_{app})$ ∂(baseline)$^{-1}$	3.2e-01 ± 5.4e-03	9.17	0.822	< 0.001
5	N_2, O_2, Ar	990	$\partial(\delta^{18}O_{app})$ ∂(baseline slope)$^{-1}$	-1.7e-01 ± 2.7e-03	9.11	0.824	< 0.001
6	N_2, O_2, Ar	990	$\partial(\delta^{18}O_{app})$ ∂(frequency scale)$^{-1}$	-1.4e03 ± 1.6e01	6.72	0.904	< 0.001
7	N_2, O_2, Ar	990	$\partial(\delta^{18}O_{app})$ ∂(free linewidth)$^{-1}$	1.4e02 ± 5.8e-01	2.54	0.986	< 0.001
8	N_2, O_2, Ar	990	$\partial(\delta^{2}H_{app})$ ∂(frequency shift)$^{-1}$	n.s.	14.1	0.966	< 0.001
9	N_2, O_2, Ar	990	$\partial(\delta^{2}H_{app})$ ∂(residuals)$^{-1}$	3.4e00 ± 1.0e-01	9.7	0.984	< 0.001
10	N_2, O_2, Ar	990	$\partial(\delta^{2}H_{app})$ ∂(baseline)$^{-1}$	-2.2e-01 ± 4.5e-03	7.7	0.990	< 0.001
11	N_2, O_2, Ar	990	$\partial(\delta^{2}H_{app})$ ∂(baseline slope)$^{-1}$	1.1e-01 ± 2.3e-03	7.7	0.990	< 0.001
12	N_2, O_2, Ar	990	$\partial(\delta^{2}H_{app})$ ∂(fixed linewidth)$^{-1}$	-8.2e03 ± 1.6e02	7.4	0.990	< 0.001
13	N_2, O_2, Ar	990	$\partial(\delta^{2}H_{app})$ ∂(frequency scale)$^{-1}$	9.8e02 ± 1.1e01	4.9	0.996	< 0.001
14	N_2, O_2, Ar	990	$\partial(\delta^{2}H_{app})$ ∂(free linewidth)$^{-1}$	-9.6e01 ± 1.0e00	4.4	0.997	< 0.001

Table 5. Comparison of empirical and semi-mechanistic models for predicting $\delta^{18}O$ and $\delta^{2}H$ values in a ternary mixture of N_2, O_2, and Ar. Overall model fit is summarized with the residual standard error (RSE), adjusted R^2 and P-value.

Model	Background	n	Response	Predictor	Model type	RSE (‰)	Adj. R^2	P-value
1	N_2, O_2, Ar	240	$\delta^{18}O_{apparent}$	$\delta^{18}O_{predicted}$	Empirical	0.99	0.988	< 0.001
2	N_2, O_2, Ar	240	$\delta^{18}O_{apparent}$	$\delta^{18}O_{predicted}$	Semi-mechanistic	1.68	0.965	< 0.001
3	N_2, O_2, Ar	240	$\delta^{2}H_{apparent}$	$\delta^{2}H_{predicted}$	Empirical	3.1	0.999	< 0.001
4	N_2, O_2, Ar	240	$\delta^{2}H_{apparent}$	$\delta^{2}H_{predicted}$	Semi-mechanistic	3.0	0.999	< 0.001
5	N_2, O_2, Ar	116	$\delta^{18}O_{apparent}$	$\delta^{18}O_{predicted}$	Empirical	0.80	0.992	< 0.001
6	N_2, O_2, Ar	116	$\delta^{18}O_{apparent}$	$\delta^{18}O_{predicted}$	Semi-mechanistic	1.21	0.982	< 0.001
7	N_2, O_2, Ar	116	$\delta^{2}H_{apparent}$	$\delta^{2}H_{predicted}$	Empirical	2.0	0.999	< 0.001
8	N_2, O_2, Ar	116	$\delta^{2}H_{apparent}$	$\delta^{2}H_{predicted}$	Semi-mechanistic	2.1	0.999	< 0.001